Data-informed statistical finite element analysis of rail buckling

Fuzheng Sun[a,*], Eky Febrianto[b,f], Heshan Fernando[c], Liam Butler[d], Fehmi Cirak[b] and Neil Hoult[a]

[a]Department of Civil Engineering, Queen's University, 58 University Ave., Kingston, K7L 3N6, ON, Canada
[b]Department of Engineering, University of Cambridge, Trumpington Street, Cambridge, CB2 1PZ, , UK
[c]Ingenuity Labs Research Institute, Queen's University, 69 Union St W, Kingston, K7L 3N6, Canada
[d]Department of Civil Engineering, York University, 4700 Keele St, Toronto, M3J 1P3, ON, Canada
[f]James Watt School of Engineering, University of Glasgow, Glasgow, G12 8QQ, UK

ARTICLE INFO

Keywords:

Distributed fiber optic sensing

Statistical finite element method

Polynomial chaos expansion

Bayesian learning

Progressive rail buckling

ABSTRACT

In this paper, the statistical finite element method is developed further towards synthesizing distributed rail response data with nonlinear finite element model predictions within and outside the measured loading range. In the data generating model of the statistical finite element method, the distributed sensing data is decomposed into finite element, model-reality mismatch, and noise components. Each component is considered uncertain and is represented as a Gaussian random vector with a corresponding prior density. The finite element prior density is updated using the Bayesian statistical framework in light of the distributed fiber optic sensing data. The calculated posterior density enables one to infer the true structural response. The required finite element prior density is determined by solving a conventional stochastic forward problem using a polynomial chaos expansion of random fields and a non-intrusive pseudo-spectral projection approach. In this research, a lab test involving a section of a rail (i.e., a beam-column structural member) instrumented with distributed fiber optic sensors and subjected to axial load causing progressive lateral buckling is considered to demonstrate the use of the statistical finite element method to improve rail response prediction. The results show improved prediction of true rail strain in linear and nonlinear regimes compared with a pure finite element model-based prediction.

1. Introduction

Railways play an essential role in the economies of many countries by facilitating the transport of goods and people. Continuously welded rail (CWR) has gradually replaced the traditional jointed rail as the preferred track type since the early 1950s due to the advantages of higher operating speeds, lower maintenance costs, increased passenger comfort, and noise reduction. However, due to the elimination of expansion joints in CWR, longitudinal compression forces develop when the track temperature exceeds the stress-free temperature (also known as the rail neutral temperature). Once the compression force in the rail exceeds a critical value, the rail will buckle, and large lateral displacements will develop that can alter the gauge of the tracks and potentially lead to a train derailment. To avoid train derailments, rail network operators do not only need to monitor the railway infrastructure continuously, but they often need to understand how the infrastructure will perform under future extreme loading events. This paper investigates the blending of DFOS measurement data with a conventional finite element (FE) model to obtain improved structural response predictions with sharp confidence bounds. To this end, the statFEM approach recently proposed by Girolami et al. [1] is used and developed further, and the theoretical derivations are validated with a lab-based rail progressive buckling test.

Traditionally, railway engineers have relied on FE modelling to help better understand the rail response under longitudinal loads and predict the critical buckling loads [2, 3, 4, 5]. FE modelling allows the rail buckling response to be studied without needing expensive and sometimes impractical experiments. Lim et al. [2] developed a three-dimensional FE model for extensive buckling analysis of a CWR track system subjected to longitudinal load,

*Corresponding authors

<18fs26@queensu.ca> (F. Sun); eky.febrianto@glasgow.ac.uk (E. Febrianto); heshan.fernando@queensu.ca (H. Fernando); liam.butler@lassonde.yorku.ca (L. Butler); fc286@cam.ac.uk (F. Cirak); neil.hoult@queensu.ca (N. Hoult)

ORCID(s): 0000-0003-0434-3265 (F. Sun); 0000-0002-9274-6904 (F. Cirak)

considering the geometrical and material nonlinearity in the FE modelling. Pucillo et al. [3] studied the thermal buckling and post-buckling responses of CWR through FE modelling and conducted sensitivity analysis to investigate the influence of critical structural parameters on the track buckling response. Kang et al. [4] investigated the rail response due to compressive axial force on ballastless track systems through both experimental investigation and FE modelling. They concluded that the rail behaviour in the lateral direction is less stiff than the longitudinal direction under axial load and that the rail deforms non-linearly and rapidly once it reaches a particular load. Miri et al. [5] used FE models to study the effect of the shape of concrete sleepers on track buckling load and concluded that the winged and frictional sleepers could provide more significant lateral resistance to the track system and hence increase the thermal buckling load capacity. These FE models involve assumptions and simplifications about the track system (e.g., the use of beam elements for modelling the rail) and estimates of the geometry (e.g., using sine curves for modelling the initial rail misalignment), material properties (e.g., elastic or elastic and perfectly plastic spring for modelling the resistance), and boundary conditions, which inevitably introduce uncertainties and inaccuracy into the FE prediction of the rail response due to the in-service operation of the railway system under the ever-changing external environment. In order to provide a predictive rail management tool, these uncertainties and inaccuracies must be accounted for when analyzing and interpreting the FE modelling results so that the potential variation in results can be quantified.

Recent advances in structural health monitoring (SHM) enable the deployment of advanced distributed sensing systems in railway infrastructure, which has introduced new opportunities for more comprehensive monitoring of the structural performance [6, 7, 8, 9, 10, 11, 12]. Compared to traditional discrete sensors, the application of distributed fiber optic sensors (DFOS) in civil engineering has overcome some disadvantages associated with traditional sensors by enabling long-distance, high-resolution, high-accuracy, durable, and robust strain measurements. The data collected from the sensors provide the actual rail response information under operational loads, which were so far interpreted or used to validate FE models for structural assessment in an ad-hoc manner to support operation and maintenance decisions [13, 14, 15]. However, this traditional approach of updating FE models using SHM data is inefficient when the amount of structural response data from advanced sensor networks is large, and the modelled structural response is complex. This has resulted in the development of data-driven approaches to directly model structural performance by learning the nonlinear mapping between the sensor data and the structural response, using machine learning and statistical learning approaches, see the recent reviews [16, 17]. Furthermore, Shen et al. [18], for instance, employed a Gaussian process regression model to directly infer rail pad and ballast stiffness using frequency response data from field hammer tests. Do et al. [19] used an artificial neural network (ANN) to directly evaluate the track modulus using the continuous deflection data from a train-mounted vertical track deflection measurement system. The fidelity of purely data-driven approaches usually depends closely on the quality of the training data, and usually, it requires large amounts of information-rich data to train a sophisticated data-driven model. The challenges associated with purely data-driven approaches have instigated research to assimilate numerical modelling based on physical laws with data-driven approaches to provide improved predictions of the structural response. Constrained Gaussian process regression with physical constraints [20, 21, 22, 23, 24] and physics-informed neural networks [25, 26, 27, 28, 29] are two typical approaches to effectively learn from limited data by explicitly taking into account the underlying physical laws governing the behaviour of structures. The mentioned methods are framed as a replacement for prevalent finite element analysis techniques and are currently only suitable for domains with elementary geometries.

In contrast, the recently proposed statistical construction of the FE method, dubbed statFEM, allows predictions to be made about the actual system behaviour in light of measurement data and a conventional FE model [1, 30]. Adopting a Bayesian viewpoint, in statFEM uncertainties in the data and model are treated as random variables with suitably chosen prior probability densities, which consolidate any knowledge available. Starting from the prior probability densities, Bayes rule provides a coherent formalism to determine their respective posterior densities while using the likelihood of the observations. An assumed statistical data generating model determines the probability or the likelihood that the model produced the observed data. See, e.g., the books [31, 32] for an introduction to Bayesian statistics and data analysis. The statFEM generating model is inspired by the seminal Kennedy and O'Hagan [33] paper on Bayesian calibration, which introduces a data-driven Gaussian process-based framework for blending data from a black-box simulator and observations. Since its inception, numerous extensions and applications of the Kennedy and O'Hagan framework have been proposed, far too many to discuss here, see e.g. [34, 35, 36, 37, 38]. A crucial component of statFEM is a random discrepancy, or misspecification, term that takes into account the mismatch between the finite element model and the actual system. In practice, such a mismatch is inevitable because of the many engineering assumptions and simplifications necessary in creating a FE model. The conditioning of the statistical statFEM model on the observation data yields a posterior probability density that consistently blends the finite element prior with the

observation data. In statFEM, the likelihood and the priors are all considered to be Gaussians so that the posterior probability a has a closed form and is a Gaussian, hence simplifying its computations.

In the original statFEM paper [1] the prior probability density of the FE solution was obtained by solving a probabilistic FE problem using a perturbation technique, which is insufficient for structures with highly nonlinear responses. Alternatively, the prior probability density can be obtained using commercially available software (e.g. Abaqus) through Monte Carlo (MC) sampling. However, in the case of rail buckling, due to the nonlinearity of the FE model, evaluating the uncertainties in the FE prediction through commercial software is extremely time-consuming and impractical. In recent years, surrogate models developed using machine learning or deep learning, such as Artificial Neural Networks (ANN) [39, 40], Gaussian processes [41, 42], Polynomial chaos expansion (PCE) [43, 44], have been increasingly used to approximate complex problems in engineering. Those surrogate models can provide sufficiently accurate results and have been used to bypass the traditional MC approach for uncertainty quantification. In the present work, a PCE-based surrogate model is constructed to approximately model the rail progressive buckling response under the axial load for fast uncertainty quantification in the modelled rail response in order to significantly reduce the computational cost of modelling the geometrical nonlinearity in the rail response. A simplified rail FE model is first established with beam elements in the commercial software (i.e., Abaqus) to generate samples to train the surrogate model. The trained surrogate model is further used to obtain the uncertainties in the modelled rail response, which are combined with the DFOS data from previously performed controlled lab rail progressive buckling experiments to enable improved predictions of rail response and buckling assessment under axial load using the data-informed statistical finite element analysis. By introducing the classical Euler-Bernoulli beam theory, the statFEM also enables the accurate prediction of lateral rail deflection, which is valuable rail response information that railway owners rely on to make decisions on railway operation and maintenance.

2. Strain data acquisition

Compared to traditional jointed rail, longitudinal compression force can be developed in the CWR due to the elimination of joints, which results in rail buckling once this load is higher than the load carrying capacity of the CWR system. In the current proof of concept work, the force in the rail was applied using an actuator rather than due to thermal effects. However, the buckling mechanisms are similar and DFOS data can be used to capture the mechanism in both cases. A 3.048 m ASCE 12 lb/yd rail was used in this work in order to limit the buckling load of the rail to an achievable level based on the available space and actuator capacity. Two different distributed fiber optic measurement systems—a long-range Brillouin-based system and a short-range, but more accurate, Rayleigh-based system—were used to measure the strains during the loading test. The following subsections describe the experimental setup, properties of the two analyzers, and the strain data set. Further details of the experiment can be found in Sun et al. [12].

2.1. Experimental test setup

The laboratory setup for the rail loading experiments is shown in Figure 1. The geometric and material properties of the ASCE 12 lb/yd rail are provided in Table 1. The rail was held in a self-reacting frame, which consisted of two steel plates that were connected by four threaded rods. The axial load was applied using an Enerpac hydraulic jack that was aligned with the instrumented rail along its neutral axis. A Strainsert universal flat load cell with a 222 kN loading capacity was connected to the hydraulic jack to measure the load applied to the rail.

Two rollers were placed at either end of the rail specimen, and the axial load was applied to the rail through the rollers enabling rotation about the weak-axis of bending but restraining rotation about the strong-axis. In all tests, the rail was also supported against strong axis buckling by two rollers at 1 m and 2 m along the length. A small amount of axial compressive load (approximately 0.4 kN) was applied to the rail before the start of the test to hold the rail in place. A linear potentiometer (LP) was installed at the rail's mid-length to measure the lateral deflection. The axial load and LP measurements were recorded using a System 7000 StrainSmart data acquisition system at a rate of 1 Hz.

A 35 m long nylon-coated fiber optic sensing cable was installed along eight different paths on the surface of the rail as shown in Figure 2b. To ensure enough data was obtained for use with the statFEM, the fiber was installed at 8 separate locations on the rail cross section (F1 to F8, as shown in Figure 2) and monitored with one of either the BOTDA or Rayleigh system (it is not possible to attach both systems to the same fiber simultaneously) to enable the strain plane at any point along the length of the rail to be fitted (see Sun et al. [12] for details). As a result of this and the

Table 1
Geometric and material properties of ASCE 12 lb/yd rail

Property	Value
Elastic modulus	207 GPa
Cross-sectional area	761 mm^2
Minimum second moment of area	53000 mm^4

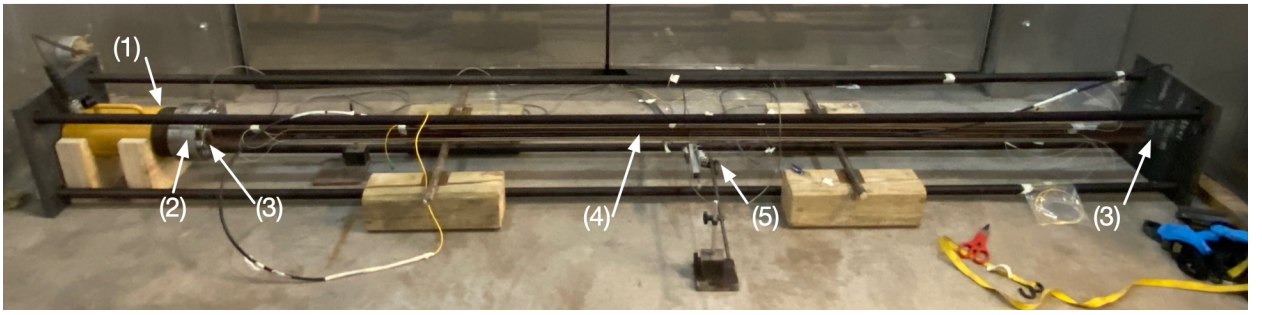

Figure 1: The setup for the pinned-pinned rail loading experiment. (1) Hydraulic Jack; (2) Load cell; (3) Pin supports; (4) Rail; (5) Linear potentiometers

fact that no two tests had the same geometric properties, as will be discussed in greater detail later, it was not possible to compare the results of the two tests directly.

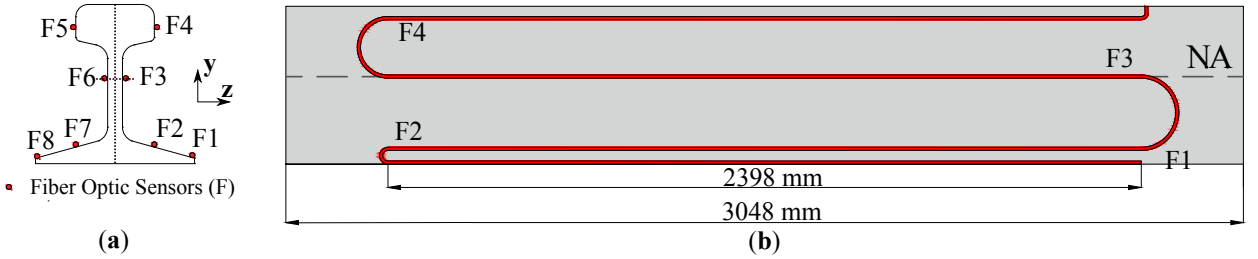

Figure 2: Schematic fiber location a) on cross-section, b) along the rail length

2.2. Measurement systems

In this study two DFOS measurement systems with different measurement precision and sensor gauge lengths were used to acquire strain data during the loading experiments. One system was the Neubrex NBX-6050A Brillouin Optical Time Domain Analysis (BOTDA) analyzer, which is referred to as the "BOTDA system" in this paper, and the second system was a LUNA ODiSI 6104 Rayleigh backscatter analyzer, which is referred to as the "Rayleigh system" in this paper. Strain measurement properties for both analyzers are provided in Table 2. The BOTDA measurements have a larger gauge length and lower measurement precision compared to the Rayleigh system; however, the BOTDA system is capable of measuring up to 100 km, which is more practical for real rail implementations.

2.3. Experiments and data sets

Two loading experiments were conducted with the instrumented rail setup: one test was conducted with the BOTDA measurement system and the second test was conducted with the Rayleigh system. In both experiments, the compressive load was applied using load steps of 1 kN until the rail buckled or the maximum strain reached 1000 microstrain ($\mu\varepsilon$) to avoid plastically deforming the rail. In this range, the non-linear response of the rail could be measured while keeping the rail within its elastic stress range to avoid causing irreversible damage. It should be noted that both tests were completed in a closed indoor environment within one hour, such that environmental changes during the test were neglectable. The rail is considered to be buckled when there is a sudden increase in the lateral deflection accompanied

Table 2
Properties of the two FOS measurement systems used in the rail loading experiments.

Property	BOTDA	Rayleigh
Sensor resolution	50 mm	2.6 mm
Measurement accuracy (1.96*σ_e)	$\pm$ 15 $\mu\varepsilon$	$\pm$ 3 $\mu\varepsilon$
Maximum sensing distance	100 km	50 m

by a drop in the axial load (explosive buckling). In a less stiff railway system, the rail is also considered to be buckled when the axial loads reach a plateau while the lateral deflections increase significantly (progressive buckling) [45]. Measurements from the load cell and LP corresponding to every DFOS sampling interval were also recorded in each test.

Figure 3 presents the axial load versus the lateral displacement at the mid-length of the rail as measured with the linear potentiometers for the two experiments. For the Rayleigh experiment, the nonlinear behaviour begins at an axial load, λ, of approximately 6 kN, whereas for the BOTDA experiment, the nonlinear behaviour begins at an axial load, λ, of approximately 10 kN. This difference in buckling respons is considered to be the result of different load eccentricities and initial geometrical imperfections in each loading experiment, as the rail needed to be reinstalled and realigned before each experiment [12]. Since the geometry changed for every test, it was not possible to conduct replicate experiments and thus only one test for each DFOS system (i.e., the BOTDA and Rayleigh system) was used in the development of the current model. As seen in Figure 3, the rail buckled at around 12 kN in the BOTDA and 11.2 kN in the Rayleigh tests, respectively. In a real railway system, the buckling load is expected to be higher due to the size of the rail and lateral resistance provided by the sleepers and ballast. Additionally, in the field the buckling load is created by restrained thermal expansion. However, the fundamental basis of the sensor system (DFOS strain measurements along the rail) and the structural behaviour (lateral weak-axis buckling) are the same in both this study and in the field. Thus, the experimental results enable the goal of this research (i.e. to perform a proof-of-concept evaluation of the application of statFEM to a non-linear structural system monitored with DFOS) to be achieved. The restraint provided by the ballast and the thermal loading effects will be considered in a future study.

Although the data at different fiber locations were collected, the data used for the statFEM analysis is the strain measured at the neutral axis for weak axis bending (F3 in Figure 2a). The strain at this location is purely due to the axial compression and weak axis bending. This strain location was chosen to avoid the need to remove the effects of strong axis bending from the measurements.

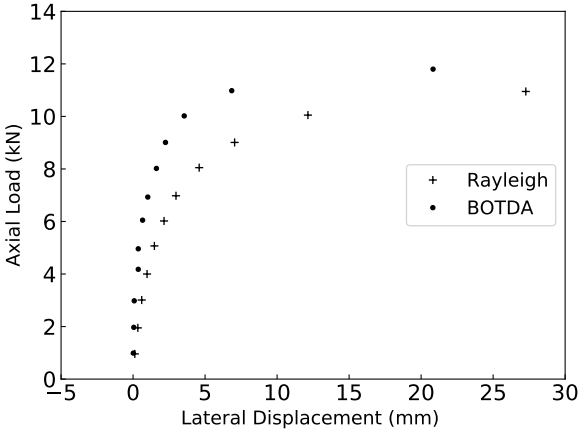

Figure 3: Axial load vs mid-length lateral displacement in compressive buckling tests.

3. Review of the statistical finite element method

In this section, the statistical finite element method (statFEM) is reviewed and its application to rail progressive buckling is discussed. To begin with, a statistical model describing the relationship between the experimental DFOS strain data and FE data is proposed. Next, the computation of the prior probability distribution of the FE data using a polynomial chaos expansion (PCE) is considered. At last, the synthesis of the DFOS strain data and the FE data using Bayes rule is described. The possibility to predict the structural response for loadings where only FE prediction but no measurements are available is highlighted.

3.1. Statistical model

As introduced in Section 2, the strain distribution along the rail specimen is determined by measuring the strains at a fixed set of sensor locations and axial loads using the DFOS sensing system. The observed strain vector $\boldsymbol{y}(\lambda)$ collects the strains at the n_y sensor locations and depends on the (scalar) axial load parameter λ. The observed strains are assumed to be additively composed of the true strains $\boldsymbol{z}(\lambda)$ and the measurement noise $\boldsymbol{e}$, i.e.,

$$\boldsymbol{y}(\lambda) = \boldsymbol{z}(\lambda) + \boldsymbol{e}\,. \tag{1}$$

The Gaussian measurement noise $\boldsymbol{e} \sim p(\boldsymbol{e}) = \mathcal{N}(\boldsymbol{0}, \sigma_e^2 \boldsymbol{I})$ is independent of the loading and the sensor locations. Furthermore, the parameter σ_e is the standard deviation suggested by the manufacturer of the DFOS sensing system and $\boldsymbol{I}$ is the identity matrix.

The unknown true strains $\boldsymbol{z}(\lambda)$ at the n_y sensor positions are assumed to be given by

$$\boldsymbol{z}(\lambda) = \boldsymbol{P}\boldsymbol{u}(\lambda) + \boldsymbol{d}(\lambda)\,, \tag{2}$$

where the matrix $\boldsymbol{P}$ projects the random FE solution $\boldsymbol{u}(\lambda)$ at the mesh nodes to the FE strains at locations corresponding to the measured strains $\boldsymbol{y}(\lambda)$. The random model-reality mismatch vector $\boldsymbol{d}(\lambda)$ takes into account the inadequacy of the FE model in reproducing the true structural response, and is assumed to have the zero-mean Gaussian probability distribution $p(\boldsymbol{d}(\lambda)) = \mathcal{N}(\boldsymbol{0}, \boldsymbol{C}_d(\lambda, \lambda))$. As to be specified in Section 3.3, the covariance matrix $\boldsymbol{C}_d(\lambda, \lambda)$ is obtained from a kernel function. The probability distribution of the FE solution $\boldsymbol{u}(\lambda)$ is approximated with the Gaussian probability distribution $p(\boldsymbol{u}(\lambda)) = \mathcal{N}(\overline{\boldsymbol{u}}(\lambda),\ \boldsymbol{C}_u(\lambda, \lambda))$ as discussed next.

3.2. Probability distribution of the finite element solution

The FE probability distribution $p(\boldsymbol{u}(\lambda))$ is one of the key components in statFEM and represents the uncertainty in the FE solution due to the known uncertainties in model parameters $\boldsymbol{\theta} \sim p(\boldsymbol{\theta})$, like load eccentricities or material properties. The probability distribution $p(\boldsymbol{u}(\lambda))$ is obtained by propagating $p(\boldsymbol{\theta})$ through the FE discretized equilibrium equations

$$\boldsymbol{G}(\boldsymbol{u}, \boldsymbol{\theta}) + \lambda \boldsymbol{F} = \boldsymbol{0}\,, \tag{3}$$

where $\boldsymbol{G}(\boldsymbol{u}, \boldsymbol{\theta})$ is the vector of the internal forces, $\boldsymbol{F}$ is the reference external force vector and λ is the scalar axial load parameter. In this paper, the FE solution $\boldsymbol{u}(\lambda_*)$ at a fixed λ_* is obtained by modelling the rail as a geometrically nonlinear beam and solving the respective equations with the commercial FE package Abaqus [46, 47]. To obtain the FE probability distribution $p(\boldsymbol{u}(\lambda_*))$ often the Monte Carlo (MC) method is employed with samples drawn from the input probability distribution $p(\boldsymbol{\theta})$. The MC method usually requires a large number of samples to obtain a good estimate for $p(\boldsymbol{u}(\lambda_*))$. Consequently, the MC approach is computationally intractable for most engineering applications requiring large FE models or nonlinear problems requiring iterative solution techniques.

Therefore, a polynomial chaos expansion (PCE) is used to approximate the uncertainties in the FE solution $\boldsymbol{u}(\lambda_*)$ at a fixed axial load parameter λ_* resulting from the uncertainties in the input parameters $\boldsymbol{\theta}$. In PCE a set of orthogonal Hermite polynomials $\left\{\boldsymbol{\Psi}_j\right\}_{j=0}^{n_P}$ is considered for approximating

$$\boldsymbol{u}(\lambda_*, \boldsymbol{\theta}) \approx \sum_{j=0}^{n_P} \boldsymbol{\alpha}_j(\lambda_*)\, \boldsymbol{\Psi}_j(\boldsymbol{\theta})\,, \tag{4}$$

where n_P is equal to the degree of the orthogonal polynomials. The unknown expansion coefficients $\left\{\boldsymbol{\alpha}_j\right\}_{j=0}^{n_P}$ are determined following a pseudo-spectral projection approach [47, 48]. Specifically, at first, a set of a few quadrature points $\left\{\boldsymbol{\theta}_k\right\}_{k=0}^{n_{\text{PCE}}}$ are sampled from the distribution $p(\boldsymbol{\theta})$, and subsequently for each $\boldsymbol{\theta}_k$ the respective finite element solution $\boldsymbol{u}(\lambda_*, \boldsymbol{\theta}_k)$ is computed. It is worth emphasizing that the total number of samples is in the order of $n_{\text{PCE}} \approx 10$, compared with tens of thousands of samples that are required in standard MC. As mentioned, each FE solution $\boldsymbol{u}(\lambda_*, \boldsymbol{\theta}_k)$ was determined with the commercial FE package Abaqus. Subsequently, the expansion coefficients $\{\boldsymbol{\alpha}_j(\lambda_*)\}$ are determined with the open-source library Chaospy [49].

Once the polynomial chaos expansion (4) is established, a large set of samples $\boldsymbol{\theta}_k \sim p(\boldsymbol{\theta})$ is sampled to determine the approximate Gaussian probability distribution $p(\boldsymbol{u}(\lambda_*)) = \mathcal{N}(\overline{\boldsymbol{u}}(\lambda_*), \boldsymbol{C}_u(\lambda_*, \lambda_*))$ by computing the empirical mean $\overline{\boldsymbol{u}}(\lambda_*)$ and covariance $\boldsymbol{C}_u(\lambda_*, \lambda_*)$ of the samples. In the present study the probability distribution $p(\boldsymbol{\theta})$ is a Gaussian and can be easily sampled.

3.3. Bayesian inference

By virtue of the postulated statistical model in Equations (1) and (2), the Gaussian approximate FE probability distribution $p(\boldsymbol{u}(\lambda_*)$ and the Gaussian model-mismatch distribution $p(\boldsymbol{d}(\lambda_*))$, the true strain probability distribution at a fixed λ_* reads

$$p(\boldsymbol{z}(\lambda_*)) = \mathcal{N}\left(\overline{\boldsymbol{z}}(\lambda_*), \boldsymbol{C}_z(\lambda_*, \lambda_*)\right) = \mathcal{N}\left(\boldsymbol{P}\overline{\boldsymbol{u}}(\lambda_*),\ \boldsymbol{P}\boldsymbol{C}_u(\lambda_*, \lambda_*)\boldsymbol{P}^{\mathsf{T}} + \boldsymbol{C}_d(\lambda_*, \lambda_*)\right)\,. \tag{5}$$

Note that this represents a prior probability distribution and is independent of measurement data.

The measured strain and axial load parameter pairs $\mathcal{Y} = \left\{\boldsymbol{y}_i, \lambda_i\right\}_{i=1}^{n_\lambda}$ are only known for n_λ distinct axial load values. The probability distribution of the true strain $\boldsymbol{z}(\lambda_*)$ at a axial load value λ_* can be determined using the Bayes formula. However, because all the involved densities are Gaussians it is more expedient to consider instead the following joint probability distribution

$$\begin{pmatrix} \boldsymbol{z}\left(\lambda_*\right) \\ \boldsymbol{y}_1 \\ \vdots \\ \boldsymbol{y}_{n_\lambda} \end{pmatrix} \sim \mathcal{N}\left(\begin{pmatrix} \boldsymbol{P}\overline{\boldsymbol{u}}\left(\lambda_*\right) \\ \boldsymbol{P}\overline{\boldsymbol{u}}\left(\lambda_1\right) \\ \vdots \\ \boldsymbol{P}\overline{\boldsymbol{u}}\left(\lambda_{n_\lambda}\right) \end{pmatrix}, \begin{pmatrix} \boldsymbol{C}_z\left(\lambda_*, \lambda_*\right) & \boldsymbol{C}_z\left(\lambda_*, \lambda_1\right) & \dots & \boldsymbol{C}_z\left(\lambda_*, \lambda_{n_\lambda}\right) \\ \boldsymbol{C}_z\left(\lambda_1, \lambda_*\right) & \boldsymbol{C}_z\left(\lambda_1, \lambda_1\right) + \sigma_e^2\boldsymbol{I} & \dots & \boldsymbol{C}_z\left(\lambda_1, \lambda_{n_\lambda}\right) \\ \vdots & \vdots & \ddots & \vdots \\ \boldsymbol{C}_z\left(\lambda_{n_\lambda}, \lambda_*\right) & \boldsymbol{C}_z\left(\lambda_{n_\lambda}, \lambda_2\right) & \dots & \boldsymbol{C}_z\left(\lambda_{n_\lambda}, \lambda_{n_\lambda}\right) + \sigma_e^2\boldsymbol{I} \end{pmatrix}\right), \tag{6}$$

and to obtain the inferred true strain probability distribution by computing the conditional distribution $p(\boldsymbol{z}_{\lambda_*}|\mathcal{Y})$ [50].

For the covariance matrices $\boldsymbol{C}_z(\lambda_i, \lambda_j) = \boldsymbol{P}\boldsymbol{C}_u(\lambda_i, \lambda_j)\boldsymbol{P}^{\mathsf{T}} + \boldsymbol{C}_d\left(\lambda_i, \lambda_j\right)$ the FE covariance matrix $\boldsymbol{C}_u\left(\lambda_i, \lambda_j\right)$ is required. As described above, the FE covariance matrix is obtained by first computing the PCE approximations $\boldsymbol{u}(\lambda_i, \boldsymbol{\theta})$ and $\boldsymbol{u}(\lambda_j, \boldsymbol{\theta})$, and subsequently calculating their empirical covariances $\boldsymbol{C}_u(\lambda_i, \lambda_j)$ using the PCE solution. The covariance matrix $\boldsymbol{C}_d\left(\lambda_i, \lambda_j\right)$ is determined from the squared exponential kernel

$$c_d\left((\boldsymbol{x}_m, \lambda_i), (\boldsymbol{x}_n, \lambda_j)\right) = \sigma_d^2 \exp\left(-\frac{\|\boldsymbol{x}_m - \boldsymbol{x}_n\|^2}{2\ell_d^2} - \frac{\|\lambda_i - \lambda_j\|^2}{2\ell_\lambda^2}\right), \tag{7}$$

where $\boldsymbol{x}_m$ and $\boldsymbol{x}_n$ denote the coordinates of the measurement locations. The scaling parameter σ_d and the length scale parameters ℓ_d and ℓ_λ are the three underlying hyperparameters of the proposed statistical model. The hyperparameters are learned from the data by minimizing the negative of the log marginal likelihood $-\log p(\mathcal{Y})$. According to Equation (6) and the marginalization property of Gaussians the marginal likelihoood is given by

$$p(\mathcal{Y}) = \mathcal{N}\left(\begin{pmatrix} \boldsymbol{P}\overline{\boldsymbol{u}}(\lambda_1) \\ \vdots \\ \boldsymbol{P}\overline{\boldsymbol{u}}\left(\lambda_{n_\lambda}\right) \end{pmatrix}, \begin{pmatrix} \boldsymbol{C}_z(\lambda_1,\lambda_1) + \sigma_e^2\boldsymbol{I} & \dots & \boldsymbol{C}_z\left(\lambda_1,\lambda_{n_\lambda}\right) \\ \vdots & \ddots & \vdots \\ \boldsymbol{C}_z\left(\lambda_{n_\lambda},\lambda_2\right) & \dots & \boldsymbol{C}_z\left(\lambda_{n_\lambda},\lambda_{n_\lambda}\right) + \sigma_e^2\boldsymbol{I} \end{pmatrix}\right). \tag{8}$$

Moreover, the inferred true strain probability distribution is given by the conditional probability distribution $p(\boldsymbol{z}_{\lambda_*}|\mathcal{Y}) = \mathcal{N}(\overline{\boldsymbol{z}}_{|\mathcal{Y}}(\lambda_*), \boldsymbol{C}_{z|\mathcal{Y}}(\lambda_*,\lambda_*)$. The conditioned mean $\overline{\boldsymbol{z}}_{|\mathcal{Y}}(\lambda_*)$ and covariance $\boldsymbol{C}_{z|\mathcal{Y}}(\lambda_*,\lambda_*)$ are obtained from Equation (6) with the aid of standard relations for Gaussian probability densities, see e.g. [51].

In summary, statFEM can be used to synthesize the FE prediction and the available monitoring data to infer true structural response of an instrumented structure. The overall procedure for implementing the statFEM is outlined in Table 3.

4. Results and discussion

In this study, the prediction of true strains for a section of rail subjected to increasing axial loads using uncertain FE predictions and the DFOS strain measurements from either BOTDA system (longer measurement length) or Rayleigh system (higher accuracy and sensor resolution) is presented. In the future field application, only the measurements from one DFOS system will be considered for the analysis. The analysis involves the distributed rail surface strain measurement from fiber F3 (see Figure 2) across multiple discrete axial loads and FE modelling of the physical test, see Section 2. All the analyses conducted in this paper are carried out using a computer with 4 cores, 8 GB Random-access memory (RAM) and an i5-1035G1 CPU.

4.1. Forward finite element prediction

In this section, the prior FE strain distribution $p(\boldsymbol{Pu})$ at the location of F3 (see Figure 2) due to randomised input parameters is presented. As mentioned in Section 3.2, Abaqus is used as the forward FE solver. Figure 4 presents the geometrical model used in the simulations. The geometry is discretised into 10 three-node quadratic beam elements (Abaqus B22 elements) with 21 nodes and 63 degrees of freedoms. The large displacement effect is considered in the analysis in order to include geometrical nonlinearity under increasing axial loads. Similar to the experimental specimen, the left end of the beam (Point A) is pinned (displacement constraint in x and y directions with free rotation), while the right end (Point B) is supported with a roller constraint (only the y displacement is constrained).

In this work uncertainty inputs with three statistically independent components $\boldsymbol{\theta} = (\delta_L, \delta_R, \kappa)$ are considered, where δ_L and δ_R denote the load eccentricities on the left and right end of the beam, respectively, and κ encapsulates the initial geometric imperfections along the rail. Specifically, the load eccentricity δ is defined as the distance between the location where the axial load is applied and the centroid of the beam's cross-section, while the initial geometrical imperfection κ represents the initial misalignment defect of the track due to manufacturing, see Figure 4. The initial geometry imperfection κ is applied by assigning the scaled first buckling mode to the geometry of the FE model. The probability distribution of the three random inputs is defined as a multivariate normal distribution where the means (in millimetres) and variances are determined empirically,

$$p(\boldsymbol{\theta}) = \mathcal{N}\left(\begin{pmatrix} 1.78 \\ 0.27 \\ -3.0 \end{pmatrix}, \begin{pmatrix} 0.5^2 & 0 & 0 \\ 0 & 0.5^2 & 0 \\ 0 & 0 & 0.5^2 \end{pmatrix}\right). \tag{9}$$

A first order Hermite polynomial was used to obtain a surrogate model for computing the FE solution $\boldsymbol{u}(\lambda_*, \boldsymbol{\theta})$ (see Equations (4)) [52]. This surrogate can approximate the probability distribution of the FE strain that one would get from a full standard MC analysis up to an error less than 1%. The explicit form of the first order PCE is $\Psi_0(\boldsymbol{\theta}) = 1$ and $\Psi_1(\boldsymbol{\theta}) = \boldsymbol{\theta} = (\delta_L, \delta_R, \kappa)$. The respective unknown coefficients associated with the first order PCE, $\boldsymbol{\alpha} := (\alpha^0, \alpha^1_{\varepsilon_L}, \alpha^1_{\varepsilon_R}, \alpha^1_{\kappa})$, are obtained through numerical integration based on Gauss quadrature. Since a first order PCE was used, a total of 8 points need to be evaluated for 3 uncertain inputs (2 Gauss quadrature points for each input).

Once the PCE surrogate is obtained, the evaluation of $\boldsymbol{u}(\lambda_*, \boldsymbol{\theta})$ becomes computationally inexpensive, allowing for evaluation with more samples. Here $n_s = 1000$ pseudo-random samples are used drawn from the joint distribution

Table 3
Summary of statFEM analysis

Input:	**Data:** DFOS strain measurements $\mathcal{Y} = \{\boldsymbol{y}_i, \lambda_i\}_{i=1}^{n_\lambda}$ at n_λ discrete load parameters; standard deviation of the measurement noise σ_e; coordinates $\mathcal{X} = \{\boldsymbol{x}_k\}_{k=1}^{n_y}$ of the n_y measurement locations. **FE model:** A geometrically nonlinear beam FE model of the rail; axial loading $\boldsymbol{F}$; probability distribution of the input parameters $p(\boldsymbol{\theta})$.
Step 1:	Establish the strain projection matrix $\boldsymbol{P}$ from the sensor coordinates $\boldsymbol{x}_i$, nodal FE coordinates and FE basis functions.
Step 2:	Determine the PCE approximations $\boldsymbol{u}(\lambda_i, \boldsymbol{\theta})$ and $\boldsymbol{u}(\lambda_*, \boldsymbol{\theta})$ in Equation (4) at the n_λ load parameter values and the load parameter of interest λ_*.
Step 3:	Calculate the empirical mean vectors $\overline{\boldsymbol{u}}(\lambda_i)$ and $\overline{\boldsymbol{u}}(\lambda_*)$, and the covariance matrices $\boldsymbol{C}_u(\lambda_i, \lambda_j)$ and $\boldsymbol{C}_u(\lambda_*, \lambda_j)$ by sampling from the PCE approximations. Note that the covariance matrices are symmetric.
Step 4:	Construct the model-reality mismatch covariance matrices $\boldsymbol{C}_d(\lambda_i, \lambda_j))$ by introducing the sensor coordinates $\boldsymbol{x}_m$ and load values λ_i into the covariance function (7).
Step 5:	Learn the values of the hyperparameters $\boldsymbol{\theta}$ by minimizing the negative log marginal likelihood $-\log p(\mathcal{Y})$.
Step 6:	Infer true probability distribution $p(\boldsymbol{z}_{\lambda_*}|\mathcal{Y}) = \mathcal{N}(\overline{\boldsymbol{z}}_{|\mathcal{Y}}(\lambda_*), \boldsymbol{C}_{z|\mathcal{Y}}(\lambda_*, \lambda_*)$ of the strains by determining the conditional distribution of the joint distribution in Equation (6).

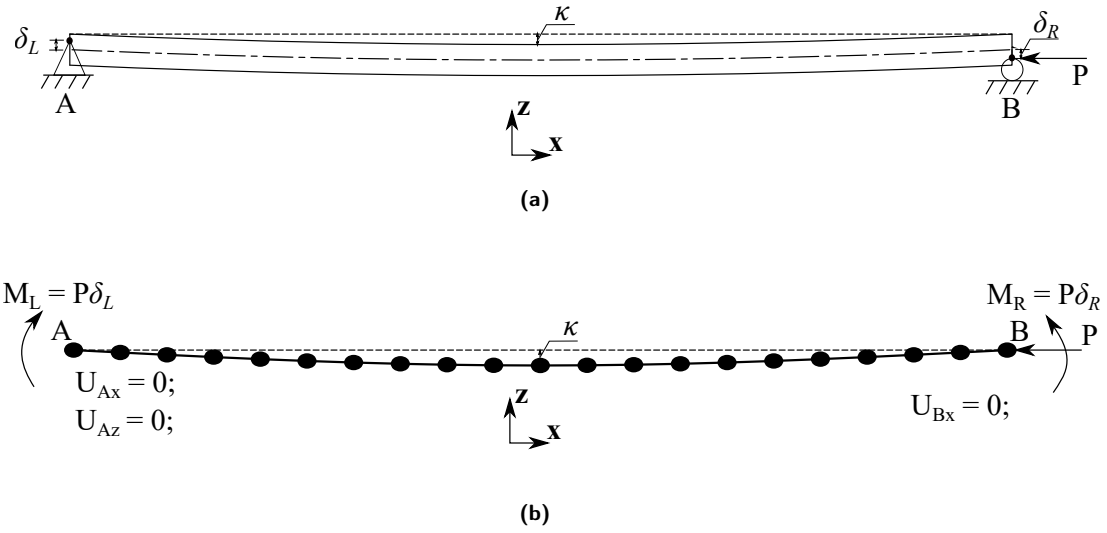

Figure 4: Mathematical model (a) of the experiments and the corresponding FE mesh (b) with the applied loading and boundary conditions.

$p(\boldsymbol{\theta})$. The Gaussian probability distribution distribution $p(\boldsymbol{Pu})$ of the FE strain can now be obtained by computing the empirical mean and covariance of the samples. Figure 5 presents the comparison of strain distribution $p(\boldsymbol{Pu}(11\,\text{kN}))$ at $x = \{0\text{ m}, 1.524\text{ m}, 3.048\text{ m}\}$ along the length of the rail evaluated with first order PCE and using the MC approach. As evident, the first order PCE produces a similar strain probability distribution at different locations in comparison with the MC results, which evaluate the strain distribution through exhaustively sampling the individual FE solution obtained with Abaqus. The average percent difference between the two methods is 0.06% in the mean $\boldsymbol{P}\overline{\boldsymbol{u}}$ and 0.5% in the standard deviation. It is worth noting that at $\lambda_* = 11$ kN the rail load deflection response is highly nonlinear and it requires approximately 54 seconds to run an individual FE analysis using Abaqus. Evaluating the probabilistic

distribution distribution of the FE strain at 11 kN using PCE takes 9 minutes and 27 seconds, which is about 100 times faster than computing $n_s = 1000$ times through MC (16 h 40 min). Therefore, in the subsequent analysis, the first order PCE will be used to evaluate the prior FE strain distribution $p(\boldsymbol{Pu})$.

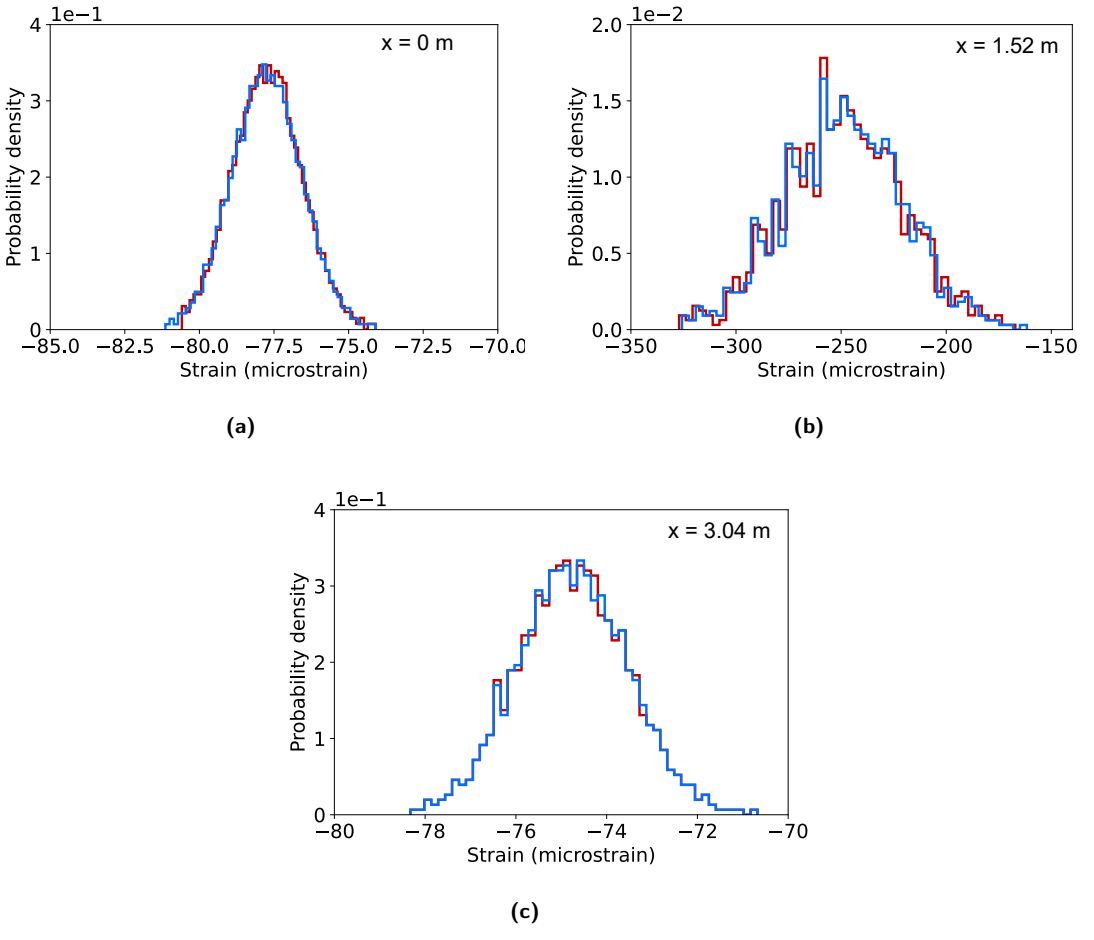

Figure 5: FE strain probability distribution at 11 kN evaluated using MC (red) and 1^{st} order PCE (blue), a) at left end, b) at mid-span, c) at right end

Figure 6 shows the comparison between the prior FE strain distribution and the experimental strain measurements obtained with the Rayleigh and BOTDA systems at axial loads λ_* between 0 kN and 11 kN. The rail enters the nonlinear regime at different loads in the two progressive buckling tests, which is thought to be the result of different initial imperfections in the two tests. According to the strain data acquired from the experiments, the rail response showed evident nonlinearity above 6 kN during the Rayleigh system test, and above 10 kN during the BOTDA system test. It is evident from Figure 6 that the prior FE strain distribution shows a good agreement with the data in the regime with less nonlinearity (below 6 kN) and deviates from the experimental data in the highly nonlinear stage (above 6 kN). Moreover, the data in the highly nonlinear regime is not captured within the 95% confidence interval of the prior FE strain distribution. This deviation clearly indicates the presence of a mismatch between the reality (experiment) and the FE model, which will be captured in the random variable $\boldsymbol{d}$ in the statistical model, see Equations (1) and (2). The use of PCE as a surrogate model to obtain the FE strain distribution can significantly decrease the computational cost while still maintaining high accuracy for the current problem. This can decrease the computational costs associated with evaluating the uncertain FE predictions to an acceptable level in order to apply the statFEM approach to practical large engineering problems.

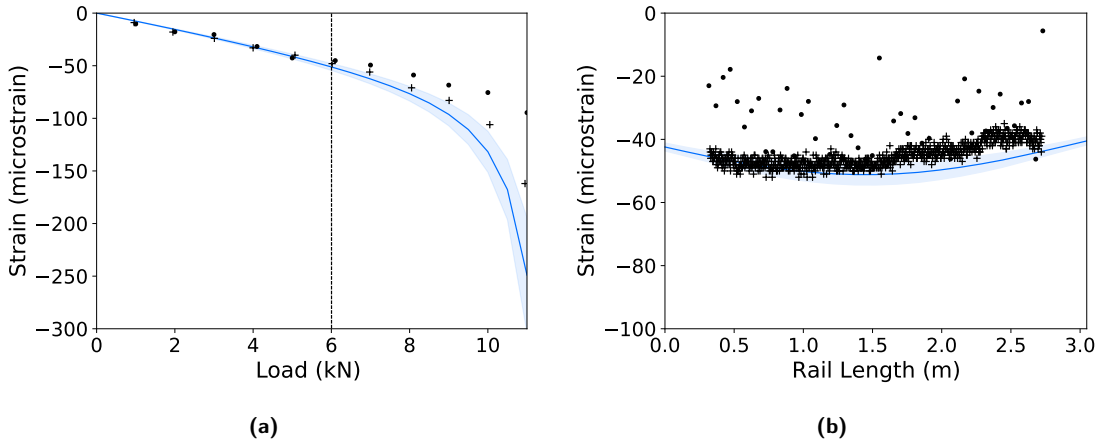

Figure 6: FE strain at the mid-length of the rail a) for axial loading from 0 kN to 11 kN, b) over the rail length at an axial load of 6 kN. The blue line represents the mean of the FE solution. The shaded area represents the 95% confidence interval. The points represent strain measurements at the mid-length of the rail ('+' for the Rayleigh system and '·' for the BOTDA system).

4.2. Prediction of rail strain in the linear regime

In a railway system, the lateral bending of the rail track under axial force is associated with rail lateral deflection, which alters the gauge distance between two adjacent rails or alignment and can potentially result in train derailment.

The true rail strain $\boldsymbol{z}(\lambda_*)$ underlying the sensor measurement at the interested axial load λ_* is unavailable and only the strain measurements at n_y locations and the corresponding n_λ axial loads pairs $\mathcal{Y}$ are available from both the Rayleigh and BOTDA measurement systems. In this section, the statFEM approach is used to infer the true rail strain distribution $p(\boldsymbol{z}|\mathcal{Y})$ at interested axial load λ_* based on the uncertain FE strain predictions $p(\boldsymbol{Pu}(\lambda_*))$, the DFOS strain measurements and the axial load parameter pairs $\mathcal{Y}$ and the corresponding uncertain FE strain predictions by determining the conditional distribution of the joint distribution in Equation (6).

4.2.1. Hyper-parameter learning

Prior to computing the inferred true strain distribution, the hyperparameters associated with the model-reality mismatch term $\boldsymbol{d}$ in the statistical model (Equation (2)) need to be derived. For the current implementation, a bivariate squared exponential kernel (Equation (7)) was used for the mismatch term $\boldsymbol{d}$ [53]. In the nonlinear regime, displacements and strains at lower axial loads λ affect the behaviour at higher axial loads. Hence, we consider a bivariate squared exponential kernel ($\boldsymbol{x}$ and λ, see Equation (7)) instead of its univariate version (only $\boldsymbol{x}$) to account for this effect. In total three hyper-parameters (σ_d, ℓ_d, ℓ_λ) are associated with the bivariate squared exponential kernel, which are collected in vector $\boldsymbol{w}$.

Before proceeding, it should be emphasized that the DFOS strain data obtained from the experiments and the corresponding n_λ axial load parameter pair $\mathcal{Y}$ were used in the hyperparameter inference. Specifically, the strain measurements obtained at particular axial loads $\lambda = \{1, 2, \ldots, 6\}$ kN were used. The choice of data constrained the rail response under chosen axial loads within the linear regime, where the strain increased linearly with the axial load. The justification of using only linear data is that in most structural monitoring applications, including rail monitoring, nonlinear response data is usually unavailable. The hyperparameter associated with the sensor measurement noise σ_e was estimated empirically using the reference strain measurement under zero load. For the Rayleigh system, the value is $\sigma_e = 1.7\mu\varepsilon$ and for BOTDA system $\sigma_e = 7.7\mu\varepsilon$ (See Table 2).

Due to the lack of information about the hyperparameters, the prior probability distribution of the hyperparameters was assumed $p(\boldsymbol{w}) \propto 1$ when inferring the $p(\boldsymbol{w}|\mathcal{Y})$, resulting into $p(\boldsymbol{w}|\mathcal{Y}) \propto p(\mathcal{Y}|\boldsymbol{w})$. The point estimation of the hyperparameters $\boldsymbol{w}$ can be obtained through either Markov chain Monte Carlo (MCMC) or optimization [1, 30]. In the current implementation, the L-BFGS-B method was used to optimize the hyperparameters, due to its efficiency and robustness in solving large-scale nonlinear problems [54]. Table 4 gives the optimized values of hyperparameters $\boldsymbol{w}$ using Rayleigh strain measurements with 400 sensors and BOTDA with 48 sensors. Once the optimal values of the

Table 4
Optimized hyper-parameters for the Rayleigh system and BOTDA system using 400 sensors and 48 sensors, respectively

	Rayleigh	BOTDA
σ_d $(\mu\epsilon)$	1.562	23.7
ℓ_d (m)	0.245	0.88
ℓ_λ (kN)	0.913	3.72
Computation time	54 min 04 sec	1 min 36 sec

hyperparameters are obtained, the true strain distribution can be inferred by conditioning on the joint distribution in Equation (6). Figure 7 shows the FE strain prediction p($\boldsymbol{u}(\lambda_*)$) and the inferred true strain prediction $p(\boldsymbol{z}_{\lambda_*}|\mathcal{Y})$ with 95% confidence interval using statFEM at interested axial load $\lambda_* = \{2, 4, 6\}$ kN for both the BOTDA system and Rayleigh system. It is evident from Figure 6 that the confidence interval of $p(\boldsymbol{z}_{\lambda_*}|\mathcal{Y})$ (grey region) obtained using the Rayleigh system is narrower than the one using the BOTDA system. One possible explanation is that the BOTDA data have less precision, and the number of data points are approximately 10 times smaller than the Rayleigh system.

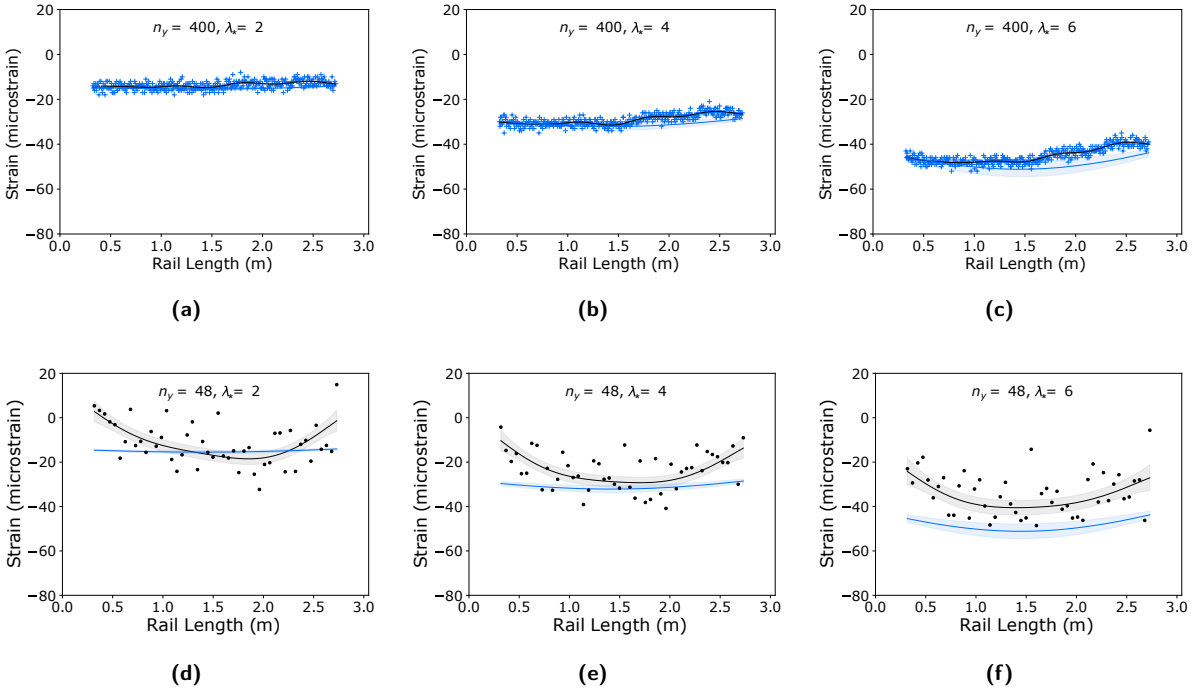

Figure 7: Inferred true rail strain with 400 sensors for Rayleigh system under axial load of a) 2 kN, b) 4 kN, c) 6 kN; and 48 sensors for BOTDA system under axial load of d) 2 kN, e) 4 kN, f) 6 kN. The blue '+' represent the Rayleigh measurements and the black '.' represent the BOTDA measurements. The blue lines represent the mean $\boldsymbol{P}\bar{\boldsymbol{u}}(\lambda_*)$ of the FE strain along the rail length, and the black lines the conditioned mean $\bar{\boldsymbol{z}}_{|\mathcal{Y}}(\lambda_*)$. The shaded areas denote the corresponding 95% confidence bounds.

4.2.2. Influence of number of sensors and strain measurement accuracy

In this section, the use of a reduced number of sensor data points to infer the true system strain $p(\boldsymbol{z}|\mathcal{Y})$ is considered, for both Rayleigh and BOTDA systems. It should be emphasised that the two DFOS measurement systems have characteristic measurement uncertainty $\sigma_e = 1.7$ $\mu\epsilon$ and $\sigma_e = 7.7$ $\mu\epsilon$ for Rayleigh and BOTDA, respectively. In practice, using reduced sensor data is desired to improve the efficiency of the overall monitoring system by reducing the cost of investment, operation, and data analysis. For this purpose, three sets of sensor clusters $n_y = \{3, 10, 40\}$ are considered to infer the true system response. Moreover, the inference for different loads $\lambda_* = \{2, 4, 6\}$ kN are also compared. As

usual, prior to the inference of the true strain $p(\boldsymbol{z}|\mathcal{Y})$, hyperparameter estimation is performed. In this set of simulations, the same set of hyperparameters (σ_d, ℓ_d, ℓ_λ) are inferred using L-BFGS-B. The point estimates of the hyperparameters for both the Rayleigh and BOTDA systems using a reduced number of sensors are shown in Table 5. According to Table 5, the value of the σ_d from the BOTDA system is much higher than that of the Rayleigh system. This is expected due to the sensor uncertainty of the BOTDA system being substantially larger than the Rayleigh system. The optimal values of ℓ_d are of similar order between the two systems. Another key observation is that as the sensor resolution increases from 10 to 40, the optimized value of ℓ_d does not change significantly. The value of ℓ_d for the Rayleigh system decreases by 50% as n_y increases from 3 to 10, while it decreases by only 20% when n_y increases from 10 to 40. In comparison, the optimized value of ℓ_d using sensor measurements from the BOTDA system varies around 1.35 as n_y increased from 10 to 40. The computational cost of optimizing the hyperparameters decreases significantly compared to the time spent on optimization using more sensors (see Table. 4), which is expected considering the reduced effort required for the matrix inversion when evaluating $p(\boldsymbol{z}|\mathcal{Y})$. The difference in runtime for the Rayleigh and BOTDA systems is considered to be the result of the different numbers of iteration steps required during the optimization as a result of different levels of precision. These findings indicate that it is possible to use a reduced number of sensors (i.e., data points) for both systems without affecting the learning of the hyperparameters.

Figure 8 and Figure 9 present the inferred true strain distribution $p(\boldsymbol{z}|\mathcal{Y})$ under interested axial load $\lambda_* = \{2, 4, 6\}$ kN using $n_y = \{3, 10, 40\}$ sensors from the Rayleigh and BOTDA measurements, respectively. As seen in Figure 8, strain prediction $p(\boldsymbol{Pu})$ is less significant at lower axial load levels. This deviation gradually increases as the axial load increases. The inferred true strain distribution using 3 sensors does not capture this deviation effectively due to the limited strain information from the 3 sensors. In comparison, the increase in the number of sensors enables a more accurate inference of the true strain response. By comparing the results for 3, 10, and 40 sensors, one can notice that the rail response using 3 sensors demonstrates a parabolic response along the rail length as the axial load increases, while the inference using 10 and 40 sensors indicates a sinusoidal rail response along the rail length. As the axial load increases, the rail response transforms from a sinusoidal to a parabolic response. The mean of the standard deviation of the inferred true strain decreases from 0.7 to 0.4. Figure 9 shows the inferred rail response using the strain data from the BOTDA system. Compared to Figure 8, the inferred strain distribution using 3 sensors has relatively large uncertainties at non-sensor locations while the uncertainty decreases with an increasing number of sensors. The increase in the number of sensors from 3 to 10 and 40 results in a decrease in the standard deviation from 6.8 to 1.2 and 1.1, respectively. It is worth noting that with a smaller number of sensors, the inferred rail response may be more influenced by individual sensor measurements. These results indicate that for both systems it is possible to use fewer sensors to obtain reliable true strain predictions, yet for the BOTDA system, fewer sensors might result in less reliable inference due to the lower precision of the measurements.

4.3. Prediction of rail strain in the nonlinear regime

When performing structural monitoring of actual rail systems, the captured strain data is usually limited to the linear regime, while data captured during the nonlinear rail response that is indicative of buckling is rarely captured. To overcome this challenge, the statistical model in Equations (1) and (2) was calibrated in the linear regime and used to extrapolate the prediction of the strain response into the interested nonlinear stage. This extrapolation is assisted with the prior FE strain distribution prediction $p(\boldsymbol{Pu})$ in the nonlinear regime (i.e., $\lambda_* > 6$ kN) obtained using the PCE as described in Section 3.2.

The predictions of the true rail strain $p(\boldsymbol{z}|\mathcal{Y})$ at the rail mid-length under axial load $\lambda_* = \{0, 1, \dots, 11\}$ kN with 95% confidence intervals using reduced number of sensors $n_y = \{3, 10, 40\}$ from the Rayleigh and BOTDA systems are presented in Figure 10. The predictive strain distribution $p(\boldsymbol{z}|\mathcal{Y})$ is evaluated based on the joint distribution in Equation (6), where the point estimates of hyperparameters for $\boldsymbol{C_d}$ obtained in Section 4.2.2 and the same strain measurements obtained at particular axial loads $\lambda = \{1, 2, \dots, 6\}$ kN were used.

As shown in Figure 10, the predictive strain with 95% confidence interval between 0 and 11 kN covers most of the strain measurements below 6 kN, and the mean strain prediction lies mostly through the mean of the data in the linear stage and close to the nonlinear FE prediction in the nonlinear regime. This is expected as only the DFOS strain measurements within the linear regime (below 6 kN) were used to calibrate the statistical model. However, a key observation is that the predictive nonlinear strain distribution inferred using statFEM deviates from the pure nonlinear FE prediction $p(\boldsymbol{Pu})$ towards the measured nonlinear response strain, due to the incorporation of the linear strain data. And with increasing number of sensors, the prediction gets closer to the measured nonlinear response strain and further from the FE prior prediction. When using the number of sensors $n_y = 40$ for the Rayleigh system, the

Table 5
Optimized hyper-parameters for the BOTDA system and Rayleigh system using reduced number of sensors $n_y = \{3, 10, 40\}$

		$\sigma_d(\mu\varepsilon)$	$\ell_d(m)$	$\ell_\lambda(kN)$	$Running\ time(sec)$
Rayleigh	$n_y = 3$	2.07	2.1	4.4	1
	$n_y = 10$	2.6	0.98	8.7	6
	$n_y = 40$	1.73	0.7	0.86	39
BOTDA	$n_y = 3$	9.12	0.363	431.2	4
	$n_y = 10$	16.9	1.35	8.98	10
	$n_y = 40$	18.47	1.38	10.23	98

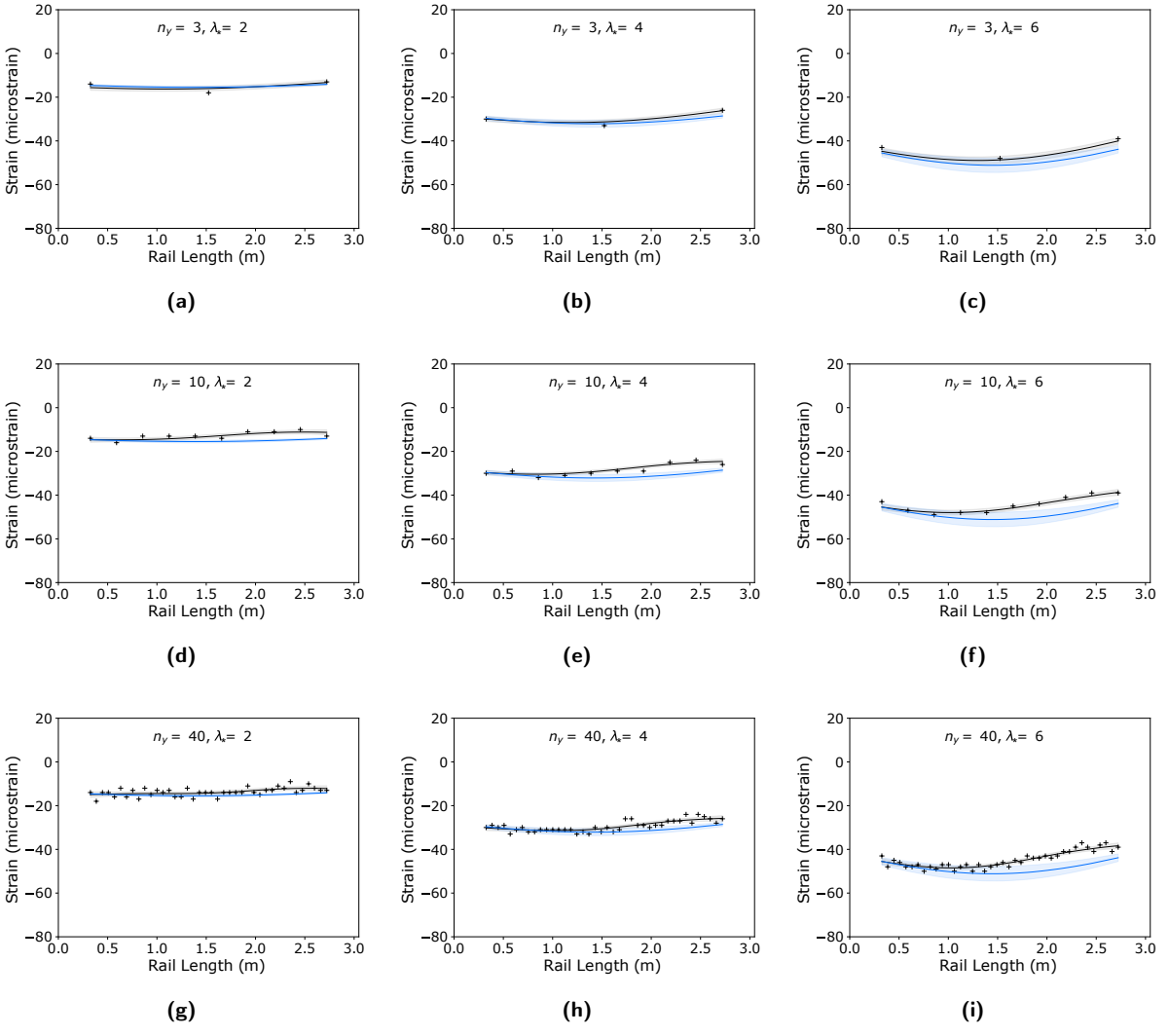

Figure 8: Inferred true rail strain with reduced number of sensors n_y for the Rayleigh system under axial load λ_* kN: a) $n_y = 3, \lambda_* = 2$, b) $n_y = 3, \lambda_* = 4$, c) $n_y = 3, \lambda_* = 6$, d) $n_y = 10, \lambda_* = 2$, e) $n_y = 10, \lambda_* = 4$, f) $n_y = 10, \lambda_* = 6$, g) $n_y = 40, \lambda_* = 2$, h) $n_y = 40, \lambda_* = 4$, i) $n_y = 40, \lambda_* = 6$. The black '+' represent the Rayleigh measurements. The blue lines represent the mean $\boldsymbol{P}\bar{\boldsymbol{u}}(\lambda_*)$ of the FE strain, and the black lines the conditioned mean $\bar{\boldsymbol{z}}_{|\mathcal{Y}}(\lambda_*)$. The shaded areas denote the corresponding 95% confidence bounds.

measured strain recorded during the nonlinear loading stage, falls within the 95% confidence interval of the predicted

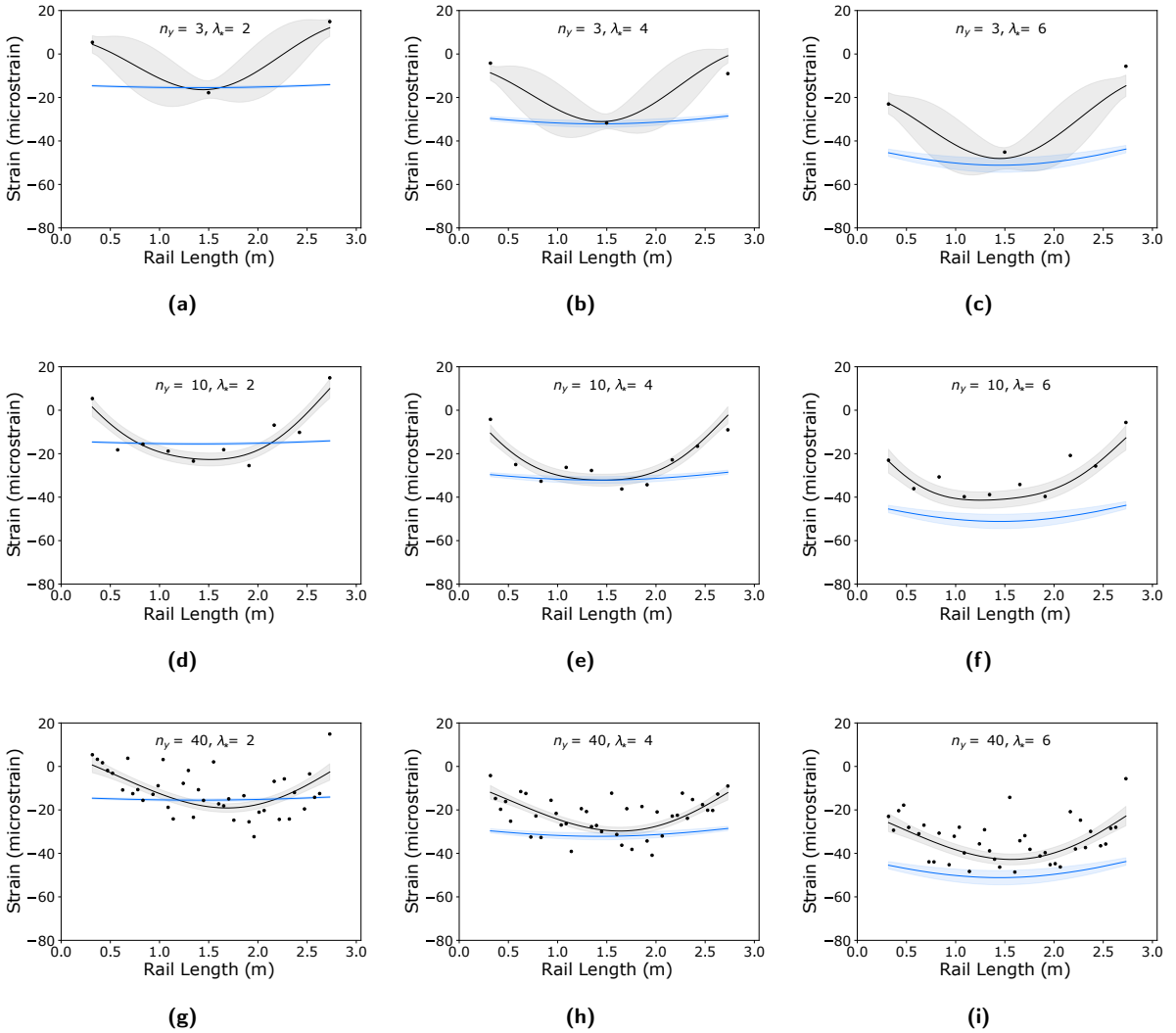

Figure 9: Inferred true rail strain with reduced number of sensors n_y for the BOTDA system under axial load λ_* kN: a) $n_y = 3, \lambda_* = 2$, b) $n_y = 3, \lambda_* = 4$, c) $n_y = 3, \lambda_* = 6$, d) $n_y = 10, \lambda_* = 2$, e) $n_y = 10, \lambda_* = 4$, f) $n_y = 10, \lambda_* = 6$, g) $n_y = 40, \lambda_* = 2$, h) $n_y = 40, \lambda_* = 4$, i) $n_y = 40, \lambda_* = 6$. The black '+' represent the Rayleigh measurements. The blue lines represent the mean $\boldsymbol{P}\bar{\boldsymbol{u}}(\lambda_*)$ of the FE strain, and the black lines the conditioned mean $\overline{\boldsymbol{z}}_{|\mathcal{Y}}(\lambda_*)$. The shaded areas denote the corresponding 95% confidence bounds.

strain. It should be noted here the real rail bending strain measurements in the nonlinear regime are not used to calibrate the statistical model and are only used to compare with the predictive nonlinear strain from statFEM. The prediction using the the number of sensors $n_y = \{3, 10, 40\}$ from the BOTDA system demonstrates similar performance to the Rayleigh system. The nonlinear predictive strain response is improved by incorporating the linear strain data into the FE prediction. The 95% confidence interval of the predictive strain for the BOTDA system is larger than that for the Rayleigh system due to the larger value of the hyperparameter σ_d for the BOTDA system. In the linear region, the strain distribution prediction using statFEM lies through the measurement data. The predictive nonlinear strain distribution is significantly improved over the FE prior prediction, although this improvement is less significant when only using 3 sensors. For $n_y = 10$ and $n_y = 40$ sensors, the predictive mean of the strain response before 9 kN agrees well with the strain measurements during the experiment. For the strain predictions made for loading between 9 and 11 kN (i.e., in the non-linear region), although the predictive mean deviates from the strain measurements due to the lack of data at those axial loads when calibrating the statistical model, the strain prediction using the statFEM and the linear strain

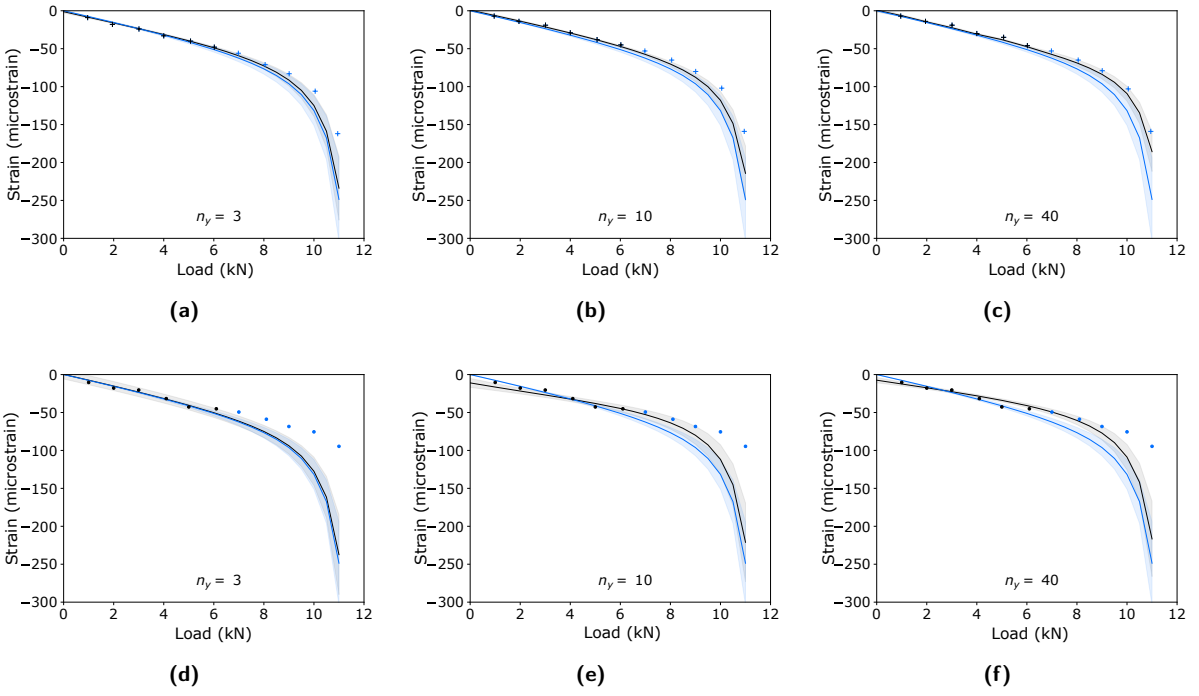

Figure 10: Predicted true strain distribution at the rail mid-length between 0-11 kN (black line + gray shaded area) based on linear strain measurements (black crossing) and nonlinear FE strain prediction (blue line + blue shaded area) using number of sensors *a)* $n_y = 3$, *b)* $n_y = 10$, *c)* $n_y = 40$ from the Rayleigh test; and *d)* $n_y = 3$, *e)* $n_y = 10$, *f)* $n_y = 40$ from the BOTDA test. The blue '+' and '.' represent the nonlinear strain measurements in the Rayleigh and BOTDA test, and are presented for comparison with the predicted true nonlinear strain distribution

response data is still better than the FE only prediction. The available data in practice is usually limited to the linear regime as most railway tracks are operated under normal (unbuckled) conditions, so using the linear data to achieve improved predictions of the nonlinear response is desired. Understanding the nonlinear rail response under potential loads is critical for helping to inform rail asset managers when to implement future maintenance and repair work. The results presented in this section indicate that the statFEM overall can provide improved prediction of nonlinear strain by synthesizing the linear measurement data and the nonlinear FE predictions, although the improvement is less significant when the number of sensors is small.

4.4. Prediction of the lateral displacement

In this section, the inferred true strain distribution from the statFEM are used to derive the rail lateral displacement. Ten thousand groups of strain profiles are sampled based on the inferred true strain distribution $p(\boldsymbol{z}|\mathcal{Y})$ at a specific axial load λ_* obtained from the statFEM in the previous sections, and the curvature profile $\boldsymbol{k}$ corresponding to each sampled strain profile $\boldsymbol{\epsilon}$ is further evaluated, based on elastic beam theory, i.e.,

$$\boldsymbol{k} = \frac{1}{y_{\text{fiber}} - y_{\text{NA}}} \left(\boldsymbol{\epsilon} - \frac{\lambda_*}{EA} \right) \tag{10}$$

where $y_{\text{fiber}} - y_{\text{NA}}$ represents the distance of fiber location away from the neutral axis (NA); λ_* represents axial load and E, A represent the elastic modulus of steel and the cross-sectional area of the rail. It should be noted here that the E, A, P, $y_{\text{fiber}} - y_{\text{NA}}$ are assumed to be deterministic.

With the curvature profile $\boldsymbol{k}$, the corresponding displacement profile $\boldsymbol{f}$ is further evaluated based on double integration of the curvature profile $\boldsymbol{k}$ using numerical trapezoid integration, assuming no boundary movement. The displacement distribution $p(\boldsymbol{f})$ is obtained through evaluating displacement profiles corresponding to sampled

curvature profiles. The predicted displacements with 95% confidence interval were compared with the actual LP measured displacements during the experiments.

Figure 11 shows the displacement mean and the 95% confidence interval. Here, the displacements at an axial load of 6 kN are taken as an example for both the Rayleigh and BOTDA systems. The actual displacements measured at the mid-length of the rail recorded by the LP are 2.2 mm and 0.66 mm, respectively. According to Figure 11 and Table 6, using a larger number of sensors (i.e., 10 and 40 sensors) overall results in the improved estimation of lateral displacement, compared with the estimation with only 3 sensors. The lateral displacements inferred using only 3 sensors fail to capture the LP measured displacements for the Rayleigh system and demonstrate a significantly higher standard deviation (i.e., lower confidence) for the BOTDA system. In comparison, the inferred lateral displacements with 95% confidence interval using 10 and 40 sensors for both the Rayleigh and BOTDA systems successfully contain the LP measured displacements at the mid-length of the rail, with the predicted mean closer to the LP measured displacements and smaller standard deviation than that of the predicted displacement with only 3 sensors. In practical operation, the CWR is considered to be at high risk of buckling once the lateral displacement reaches the critical value (i.e., 12 mm), above which substantial track maintenance work and optimal operational decision would be required to prevent track buckling. The inferred true strain distribution using the statFEM enabled accurate displacement evaluations with the inherent uncertainties from the sensor measurements and FE predictions, although the confidence is lower when the smaller number of sensors is used in statFEM. The inferred displacement with 95% confidence interval enables buckling assessment and track maintenance to be undertaken with greater confidence.

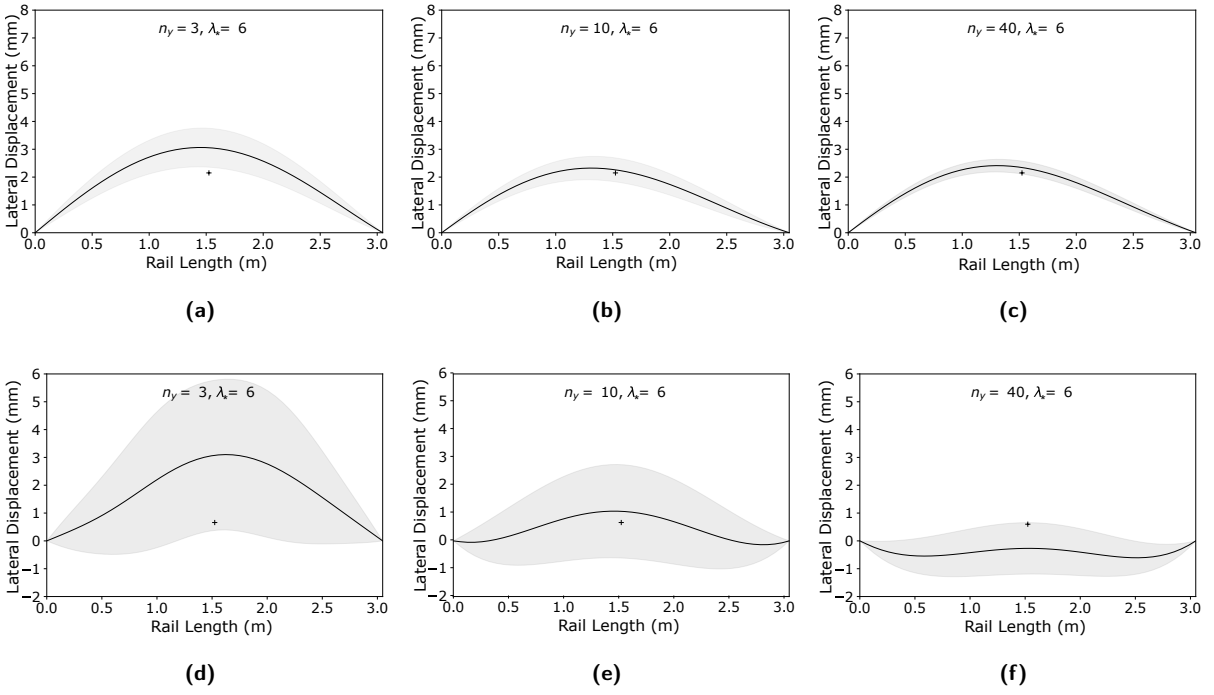

Figure 11: Lateral displacement probability distribution evaluated from inferred posterior true strain probability distribution for the Rayleigh system with the number of sensors *a)* $n_y = 3$, *b)* $n_y = 10$, *c)* $n_y = 40$; and for the BOTDA system with the number of sensors *d)* $n_y = 3$, *e)* $n_y = 10$, *f)* $n_y = 40$. The black line represents the inferred mean of displacement and the gray area represents the 95% percent of confidence interval, compared with the actual displacement '+' measured during the experiments with LP

4.5. StatFEM using pre-processed data

The above analysis presents the inferred true strain distribution from statFEM using the distributed strain measurement from a single fiber F3 (see Figure 2) and the corresponding FE strain distribution. The lateral displacement distribution is evaluated from the inferred true strain distribution, see Section 4.4. However, due to the limited strain

Table 6
Mid-length lateral displacement prediction using inferred true strain distribution from the statFEM analysis (in millimetres))

		Predicted displacement	standard deviation	Difference from LP measurements
Rayleigh	$n_y = 3$	2.8	0.46	0.6
	$n_y = 10$	2.21	0.21	0.01
	$n_y = 40$	2.25	0.15	0.05
BOTDA	$n_y = 3$	3.09	1.39	2.43
	$n_y = 10$	1.08	0.87	0.42
	$n_y = 40$	-0.27	0.49	0.93

information provided by a single fiber, one has to incorporate other information (i.e., the value of axial loads and the coordinates of the fiber) to obtain the curvature and displacement, which inevitably induces uncertainties when evaluating the curvature and displacement. Failing to consider those uncertainties would result in a deviation between the predicted displacement means and the actual displacement (see Figure 11 d, e, f). One way to avoid considering the uncertainties in axial loads and the fiber coordinates is to use the curvature data in statFEM obtained from pre-processing of the strain data from multiple fiber measurements. With more strain measurements from multiple fibers (F1 to F8, see Figure 2), one can pre-process the strain measurements of the fibers (at least three fibers) to derive the curvature data including noise along the rail length [12]. This section presents the use of curvature data with noise and prior distribution of FE bending curvature in statFEM to infer true rail bending curvature and lateral displacement distribution at 6 kN. As the curvature is derived from pre-processing strain data from multiple fibers, the standard deviation of the noise σ_e in the curvature data is not directly available from the manufacturer, hence it needs to be treated as another hyper-parameter that has to be derived from the data. The PCE is used again to approximate the prior FE curvature distribution, and the data used in statFEM is the DFOS curvature data with noise from pre-processing of strain measurements of F1-F8. The same process of statFEM analysis introduced in Section 4.2 is used to obtain the inferred true bending curvature using the curvature data with noise from the experiments conducted with the Rayleigh system and BOTDA system, respectively.

Figure 12 presents the inferred true bending curvature distribution obtained through statFEM using curvature data from $n_y = \{3,\ 10,\ 40\}$ sensors in the experiment conducted with the Rayleigh system and BOTDA system, respectively. As seen in Figure 12, the inferred mean of the true bending curvature passes through the mean of the data and the 95% confidence interval covers the variation of the data due to noise from its mean for both systems. As the number of sensors n_y increases from 3 to 10 to 40, the standard deviation of inferred true curvature distribution of the Rayleigh system gradually decreases from 0.39 km^{-1} to 0.26 km^{-1} to 0.09 km^{-1}, indicating the decreased uncertainties in the inferred true curvature distribution as the number of sensors increases. In comparison, the standard deviation of the inferred true curvature distribution for the BOTDA system does not demonstrate significant change as the number of sensors n_y increases, with the standard deviation changing from 0.47 km^{-1} to 0.62 km^{-1} to 0.56 km^{-1}. Overall, the standard deviation of the inferred true curvature distribution decreases as the number of sensors increases.

Figure 13 presents the inferred lateral displacement with 95% confidence interval at an axial load of 6 kN obtained using the inferred true curvature distribution from statFEM, and Table 7 summarizes the inferred mean and standard deviation of the lateral displacement. As seen in Figure 13, the probabilistic distribution of lateral displacement with 95% confidence interval can successfully capture the the LP measured displacement. The difference between the mean of the inferred lateral displacement at the mid-length and the LP measured displacement are within 0.13 mm for the Rayleigh system and 0.30 mm for the BOTDA system. As the number of sensors n_y increases from 3 to 10 to 40, the standard deviation for the lateral displacement for the Rayleigh test decreases from 0.45 mm to 0.3 mm to 0.1 mm. In comparison, the standard deviation for the BOTDA test varies from 0.54 to 0.73 to 0.66 as the number of sensors increased from 3 to 10 to 40. Generally, the lateral displacement with 95% confidence bound integrated using the inferred true curvature distribution in the test with the Rayleigh system shows a smaller level of uncertainty than that with the BOTDA system, which is expected considering the higher precision of the Rayleigh system versus the BOTDA system. Figure 12 and Figure 13 show that with pre-processing curvature data from multiple fiber measurements, using 3 curvature data points only can provide a good inference of the true curvature and lateral displacement. Using more than 10 sensors does not significantly influence the mean of the inferred true curvature and lateral displacement but generally does decrease their standard deviation, although the decrease is less significant for the BOTDA system due to its low precision.

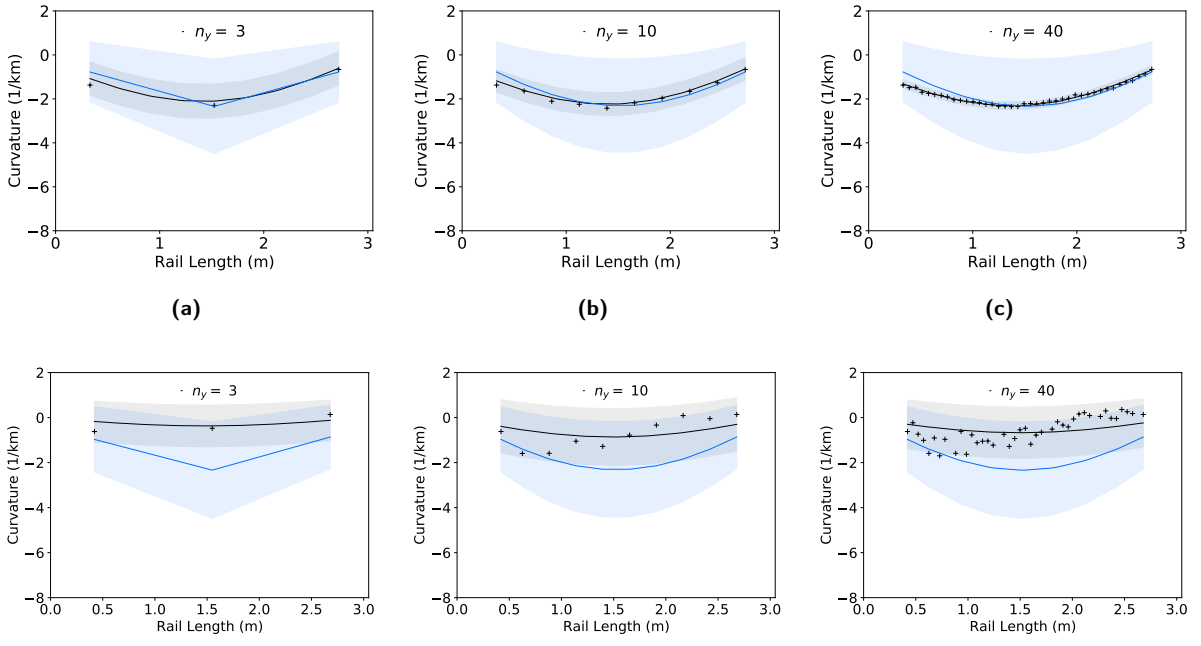

Figure 12: The inferred true curvature distribution at axial load $\lambda_* = 6$ kN for the Rayleigh system with the number of sensors a) $n_y = 3$, b) $n_y = 10$, c) $n_y = 40$; and for the BOTDA system with the number of sensors d) $n_y = 3$, e) $n_y = 10$, f) $n_y = 40$; the blue line and blue shaded area represent the FE curvature prior $p(\boldsymbol{k})$ with 95% confidence interval; the black line and gray shadow area represents the inferred FE curvature prior; the black crossing '+' represents the curvature data used for updating

Table 7
Mid-length lateral displacement prediction using inferred true strain distribution from the statFEM analysis (in millimetres))

		Predicted displacement	standard deviation	Difference from LP measurements
Rayleigh	$n_y = 3$	2.02	0.45	0.18
	$n_y = 10$	2.15	0.30	0.05
	$n_y = 40$	2.23	0.10	0.03
BOTDA	$n_y = 3$	0.35	0.54	0.31
	$n_y = 10$	0.87	0.73	0.21
	$n_y = 40$	0.63	0.66	0.03

5. Conclusions

In this paper the use of the statFEM with DFOS data measured wintin the linear range to infer and predict structural response in both the linear and non-linear range is demonstrated for the first time. The use of DFOS measurements from a rail buckling experiment is used to demonstrate the approach. By synthesizing available distributed fiber optic sensor strain (DFOS) data and an uncalibrated FE model predictions, statFEM provides a principled approach that leverages both monitoring data and a physcial model to achieve better rail strain and lateral displacement predictions. Based on the results presented in this study, the following conclusions can be drawn:

1. Polynomial Chaos Expansion (PCE) provides an accurate and computationally efficient way to obtain the prior FE probability distribution (while accounting for the relative levels of uncertainties from the governing FE model parameters), especially for large nonlinear FE models. For the lab model discussed in this paper, using PCE as a surrogate model significantly decreased the computational time using versus Monte Carlo (MC) simulation

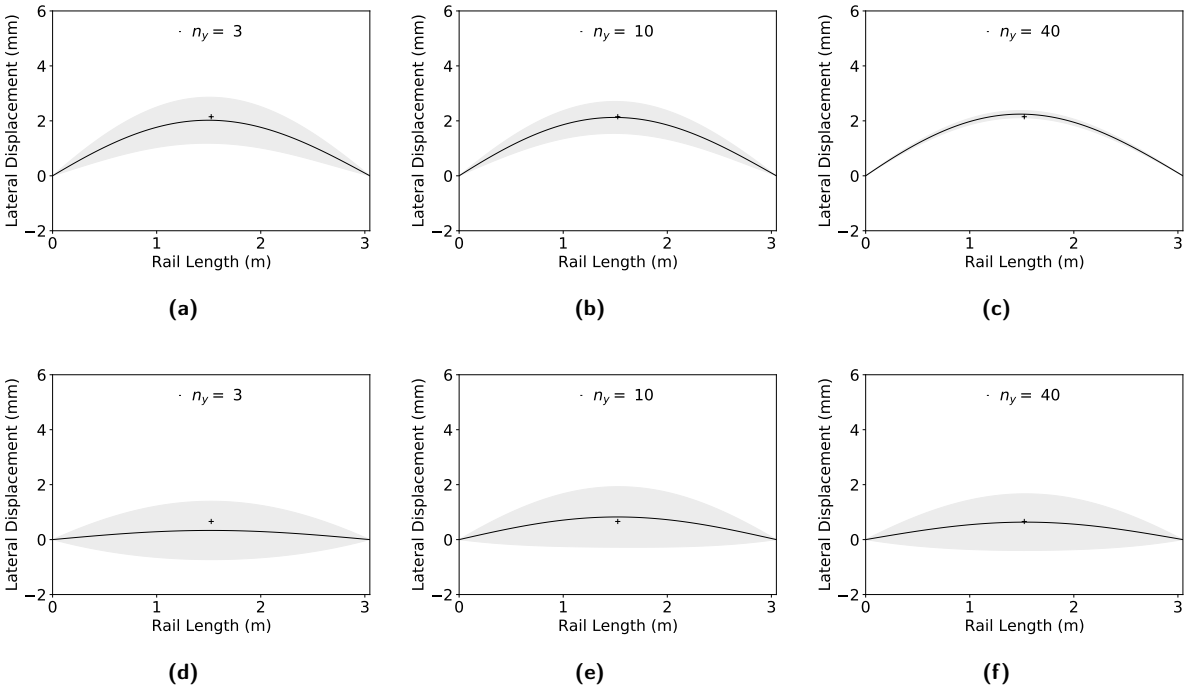

Figure 13: Inferred lateral displacement at axial load $\lambda = 6$ kN evaluated from inferred posterior curvature probability distribution for the Rayleigh test with number of sensors, a) $n_y = 3$, b) $n_y = 10$, c) $n_y = 40$; and for the BOTDA test with number of sensors, d) $n_y = 3, e$) $n_y = 10, f$) $n_y = 40$. The black line represents the inferred mean of lateral displacement and the gray area represents the 95% percent of confidence interval, compared with the actual displacement ('+') measured during the experiment with LP

from 16 h 40 min to 9 min. The accuracy of the mean and standard deviation was maintained to within 99.94% and 99.50% compared with the mean and standard deviation evaluated from MC simulation.

2. The effect of both the number of sensing points included and the accuracy of the sensor measurements on the statFEM results were evaluated by considering reduced numbers of sensors $n_y = \{3, 10, 40\}$. The use of higher accuracy measurements and more sensors enables a more detailed response to be inferred and also decreases the associated uncertainty bounds. However, the confidence interval decreased less significantly when considering a larger number of sensing points, indicating that even for a reduced number of sensing points, adequate rail response inference can still be achieved.
3. By employing the statFEM, it was possible to improve the predictions of rail strains in the nonlinear loading regime. StatFEM provided improved predictions by synthesizing the strain measurement data captured in the linear loading regime with the non-linear FE model predictions, compared to the predictions from the nonlinear FE model alone. Although the prediction deviates from the experimental measurements as the extrapolation gradually deviates from the training data, the use of a larger number of sensors tends to result in improved predictions that are closer to the measured nonlinear strain for both of the DFOS sensing systems used in this study.
4. The results from statFEM enabled the evaluation of the lateral displacement along the rail and its corresponding levels of uncertainty. The evaluation of the lateral displacement was affected by the number of sensors included and the accuracy of the sensing systems. Compared with using the same number of sensors for the BOTDA sensing system, the Rayleigh sensing system measurements, with their relatively higher accuracy, resulted in a reduced area of the 95% confidence bounds in the inferred lateral displacement (i.e., improved confidence) and in mean predictions which more closely matched the LP measurements

The results of this research have highlighted the application of statFEM for rail strain and displacement predictions for the purpose of buckling evaluation. Building on the Bayesian framework, the statFEM enables the fusion of data

from different sources and accuracy (i.e., sensor data and modeling data) for the improved prediction of true structural response. As the first step toward constructing a digital twin of an existing railway system, this paper presented the challenges associated with the application of statFEM to evaluating rail systems monitored using DFOS and offered several solutions. In future work, the influence of temperature on longitudinally restrained rail systems will be incorporated into both lab tests and the accompanying statFEM models. After this further evaluation work is conducted, a digital twin of an existing railway system will be constructed to help significantly improve current railway monitoring and buckling evaluation processes.

Declaration of Competing Interest

The authors have no conflict of interest / competing interests.

Acknowledgements

This project was supported in part by collaborative research funding from the National Research Council of Canada's Artificial Intelligence for Logistics Program. This research was also supported by the Natural Sciences and Engineering Research Council of Canada and Transport Canada. The authors also appreciate the support of Merrina Zhang, Alireza Roghani, and Robert Caldwell from National Research Council.

References

[1] M. Girolami, E. Febrianto, G. Yin, F. Cirak, The statistical finite element method (statFEM) for coherent synthesis of observation data and model predictions, Computer Methods in Applied Mechanics and Engineering 375 (2021) 113533:1–113533:32. doi:https://doi.org/10.1016/j.cma.2020.113533.

[2] N.-H. Lim, N.-H. Park, Y.-J. Kang, Stability of continuous welded rail track, Computers & Structures 81 (2003) 2219–2236. doi:https://doi.org/10.1016/S0045-7949(03)00287-6.

[3] G. P. Pucillo, Thermal buckling and post-buckling behaviour of continuous welded rail track, Vehicle System Dynamics 54 (2016) 1785–1807. doi:https://doi.org/10.1080/00423114.2016.1237665.

[4] C. Kang, M. Bode, M. Wenner, S. Marx, Experimental and numerical investigations of rail behaviour under compressive force on ballastless track systems, Engineering Structures 197 (2019) 109413. doi:https://doi.org/10.1016/j.engstruct.2019.109413.

[5] A. Miri, J. A. Zakeri, D. Thambiratnam, T. Chan, Effect of shape of concrete sleepers for mitigating of track buckling, Construction and Building Materials 294 (2021) 123568. doi:https://doi.org/10.1016/j.conbuildmat.2021.123568.

[6] P. Wang, K. Xie, L. Shao, L. Yan, J. Xu, R. Chen, Longitudinal force measurement in continuous welded rail with bi-directional FBG strain sensors, Smart Materials and Structures 25 (2015) 015019. doi:10.1088/0964-1726/25/1/015019.

[7] L. J. Butler, W. Lin, J. Xu, N. Gibbons, M. Z. Elshafie, C. R. Middleton, Monitoring, modeling, and assessment of a self-sensing railway bridge during construction, Journal of Bridge Engineering 23 (2018) 04018076. doi:10.1061/(ASCE)BE.1943-5592.0001288.

[8] M. Qiushi, G. Xiaorong, Z. Hongna, W. Zeyong, Z. Quanke, Composite railway health monitoring system based on fiber optic bragg grating sensing array, in: 2014 IEEE Far East Forum on Nondestructive Evaluation/Testing, IEEE, 2014, pp. 259–264. doi:10.1109/FENDT.2014.6928276.

[9] L. N. Wheeler, W. A. Take, N. A. Hoult, H. Le, Use of fiber optic sensing to measure distributed rail strains and determine rail seat forces under a moving train, Canadian Geotechnical Journal 56 (2019) 1–13. doi:https://doi.org/10.1139/cgj-2017-0163.

[10] L. N. Wheeler, E. Pannese, N. A. Hoult, W. A. Take, H. Le, Measurement of distributed dynamic rail strains using a rayleigh backscatter based fiber optic sensor: Lab and field evaluation, Transportation Geotechnics 14 (2018) 70–80. doi:https://doi.org/10.1016/j.trgeo.2017.10.002.

[11] C. Barker, N. A. Hoult, M. Zhang, Development of an axial strain measurement system for rails, Journal of Performance of Constructed Facilities 35 (2021) 04020145. doi:10.1061/(ASCE)CF.1943-5509.0001559.

[12] F. Sun, N. A. Hoult, L. J. Butler, M. Zhang, Distributed monitoring of rail lateral buckling under axial loading, Journal of Civil Structural Health Monitoring (2021) 1–18. doi:https://doi.org/10.1007/s13349-021-00504-w.

[13] R. Pimentel, D. Ribeiro, L. Matos, A. Mosleh, R. Calçada, Bridge weigh-in-motion system for the identification of train loads using fiber-optic technology, in: Structures, volume 30, Elsevier, 2021, pp. 1056–1070. doi:https://doi.org/10.1016/j.istruc.2021.01.070.

[14] C. Ye, L. Butler, F. Huseynov, C. Middleton, Evaluating in-service structural behaviour of an operational railway bridge using fibre optic sensing and structural model updating, Engineering Structures 247 (2021) 113116. doi:https://doi.org/10.1016/j.engstruct.2021.113116.

[15] J. Xu, L. J. Butler, M. Z. Elshafie, Experimental and numerical investigation of the performance of self-sensing concrete sleepers, Structural health monitoring 19 (2020) 66–85. doi:https://doi.org/10.1177/1475921719834450.

[16] M. Azimi, A. D. Eslamlou, G. Pekcan, Data-driven structural health monitoring and damage detection through deep learning: State-of-the-art review, Sensors 20 (2020) 2778. doi:10.3390/s20102778.

[17] L. Sun, Z. Shang, Y. Xia, S. Bhowmick, S. Nagarajaiah, Review of bridge structural health monitoring aided by big data and artificial intelligence: From condition assessment to damage detection, Journal of Structural Engineering 146 (2020) 04020073. doi:10.1061/(ASCE)ST.1943-541X.0002535.

[18] C. Shen, R. Dollevoet, Z. Li, Fast and robust identification of railway track stiffness from simple field measurement, Mechanical Systems and Signal Processing 152 (2021) 107431. doi:https://doi.org/10.1016/j.ymssp.2020.107431.
[19] N. T. Do, M. Gül, S. F. Nafari, Continuous evaluation of track modulus from a moving railcar using ANN-based techniques, Vibration 3 (2020) 149–161. doi:https://doi.org/10.3390/vibration3020012.
[20] T. Graepel, Solving noisy linear operator equations by Gaussian processes: Application to ordinary and partial differential equations, in: ICML, volume 3, 2003, pp. 234–241.
[21] S. Särkkä, Linear operators and stochastic partial differential equations in gaussian process regression, in: International Conference on Artificial Neural Networks, 2011, pp. 151–158. doi:10.1007/978-3-642-21738-8.
[22] M. Raissi, P. Perdikaris, G. E. Karniadakis, Machine learning of linear differential equations using gaussian processes, Journal of Computational Physics 348 (2017) 683–693. doi:10.1007/978-3-642-21738-8.
[23] M. Raissi, G. E. Karniadakis, Hidden physics models: Machine learning of nonlinear partial differential equations, Journal of Computational Physics 357 (2018) 125–141. doi:https://doi.org/10.1016/j.jcp.2017.11.039.
[24] A. Gregory, F. D.-H. Lau, M. Girolami, L. J. Butler, M. Z. Elshafie, The synthesis of data from instrumented structures and physics-based models via gaussian processes, Journal of Computational Physics 392 (2019) 248–265. doi:https://doi.org/10.1016/j.jcp.2019.04.065.
[25] I. E. Lagaris, A. Likas, D. I. Fotiadis, Artificial neural networks for solving ordinary and partial differential equations, IEEE Transactions on Neural Networks 9 (1998) 987–1000. doi:10.1109/72.712178.
[26] J. Han, A. Jentzen, W. E, Solving high-dimensional partial differential equations using deep learning, Proceedings of the National Academy of Sciences 115 (2018) 8505–8510. doi:https://doi.org/10.1073/pnas.171894211.
[27] M. Raissi, P. Perdikaris, G. E. Karniadakis, Physics-informed neural networks: A deep learning framework for solving forward and inverse problems involving nonlinear partial differential equations, Journal of Computational Physics 378 (2019) 686–707. doi:https://doi.org/10.1016/j.jcp.2018.10.045.
[28] L. Lu, X. Meng, Z. Mao, G. E. Karniadakis, Deepxde: A deep learning library for solving differential equations, SIAM Review 63 (2021) 208–228. doi:https://doi.org/10.1137/19M1274067.
[29] L. Yang, X. Meng, G. E. Karniadakis, B-PINNs: Bayesian physics-informed neural networks for forward and inverse pde problems with noisy data, Journal of Computational Physics 425 (2021) 109913. doi:https://doi.org/10.1016/j.jcp.2020.109913.
[30] E. Febrianto, L. Butler, M. Girolami, F. Cirak, Digital twinning of self-sensing structures using the statistical finite element method, Data-Centric Engineering 3 (2022). doi:https://doi.org/10.1017/dce.2022.28.
[31] D. Barber, Bayesian Reasoning and Machine Learning, Cambridge University Press, 2012.
[32] A. Gelman, J. B. Carlin, H. S. Stern, D. B. Dunson, A. Vehtari, D. B. Rubin, Bayesian Data Analysis, third ed., CRC Press, 2014.
[33] M. C. Kennedy, A. O'Hagan, Bayesian calibration of computer models, Journal of the Royal Statistical Society: Series B (Statistical Methodology) 63 (2001) 425–464. doi:https://doi.org/10.1111/1467-9868.00294.
[34] D. Higdon, M. Kennedy, J. C. Cavendish, J. A. Cafeo, R. D. Ryne, Combining field data and computer simulations for calibration and prediction, SIAM Journal on Scientific Computing 26 (2004) 448–466. doi:https://doi.org/10.1137/S1064827503426693.
[35] M. J. Bayarri, J. O. Berger, R. Paulo, J. Sacks, J. A. Cafeo, J. Cavendish, C.-H. Lin, J. Tu, A framework for validation of computer models, Technometrics 49 (2007) 138–154. doi:https://doi.org/10.1198/004017007000000092.
[36] Y. Xiong, W. Chen, K.-L. Tsui, D. W. Apley, A better understanding of model updating strategies in validating engineering models, Computer Methods in Applied Mechanics and Engineering 198 (2009) 1327–1337. doi:https://doi.org/10.1198/004017007000000092.
[37] X. Yang, D. Barajas-Solano, G. Tartakovsky, A. M. Tartakovsky, Physics-informed cokriging: A gaussian-process-regression-based multifidelity method for data-model convergence, Journal of Computational Physics 395 (2019) 410–431. doi:https://doi.org/10.1016/j.jcp.2019.06.041.
[38] C. Jiang, Z. Hu, Y. Liu, Z. P. Mourelatos, D. Gorsich, P. Jayakumar, A sequential calibration and validation framework for model uncertainty quantification and reduction, Computer Methods in Applied Mechanics and Engineering 368 (2020) 113172:1–113172:30. doi:https://doi.org/10.1016/j.cma.2020.113172.
[39] B.-T. Cao, M. Obel, S. Freitag, P. Mark, G. Meschke, Artificial neural network surrogate modelling for real-time predictions and control of building damage during mechanised tunnelling, Advances in Engineering Software 149 (2020) 102869. doi:https://doi.org/10.1016/j.advengsoft.2020.102869.
[40] X. Han, H. Xiang, Y. Li, Y. Wang, Predictions of vertical train-bridge response using artificial neural network-based surrogate model, Advances in Structural Engineering 22 (2019) 2712–2723. doi:https://doi.org/10.1177/1369433219849809.
[41] T. J. Santner, B. J. Williams, W. I. Notz, B. J. Williams, The design and analysis of computer experiments, Springer, 2003.
[42] M. A. Bessa, P. Glowacki, M. Houlder, Bayesian machine learning in metamaterial design: fragile becomes supercompressible, Advanced Materials 31 (2019) 1904845:1–1904845:6. doi:https://doi.org/10.1002/adma.201904845.
[43] M. A. Hariri-Ardebili, B. Sudret, Polynomial chaos expansion for uncertainty quantification of dam engineering problems, Engineering Structures 203 (2020) 109631. doi:https://doi.org/10.1016/j.engstruct.2019.109631.
[44] P. Ni, Y. Xia, J. Li, H. Hao, Using polynomial chaos expansion for uncertainty and sensitivity analysis of bridge structures, Mechanical Systems and Signal Processing 119 (2019) 293–311. doi:https://doi.org/10.1016/j.ymssp.2018.09.029.
[45] A. Kish, G. Samavedam, et al., Track buckling prevention: theory, safety concepts, and applications, Technical Report, John A. Volpe National Transportation Systems Center (US), Washington D.C., 2013.
[46] R. Y. Rubinstein, D. P. Kroese, Simulation and the Monte Carlo method, volume 10, John Wiley & Sons, 2016. doi:10.1002/9781118631980.
[47] D. Gottlieb, S. A. Orszag, Numerical analysis of spectral methods: theory and applications, SIAM, 1977. doi:https://doi.org/10.1137/1.9781611970425.
[48] D. Xiu, Numerical methods for stochastic computations: a spectral method approach, Princeton University Press, 2010. doi:https://doi.org/10.1515/9781400835348.

[49] J. Feinberg, H. P. Langtangen, Chaospy: An open source tool for designing methods of uncertainty quantification, Journal of Computational Science 11 (2015) 46–57. doi:https://doi.org/10.1016/j.jocs.2015.08.008.
[50] C. E. Rasmussen, Gaussian processes in machine learning, in: Summer school on machine learning, Springer, 2003, pp. 63–71.
[51] C. K. I. Williams, C. E. Rasmussen, Gaussian processes for machine learning, MIT Press, 2006.
[52] N. Wiener, The homogeneous chaos, American Journal of Mathematics 60 (1938) 897–936. doi:https://doi.org/10.2307/2371268.
[53] E. Schulz, M. Speekenbrink, A. Krause, A tutorial on gaussian process regression: Modelling, exploring, and exploiting functions, Journal of Mathematical Psychology 85 (2018) 1–16. doi:https://doi.org/10.1016/j.jmp.2018.03.001.
[54] C. Zhu, R. H. Byrd, P. Lu, J. Nocedal, Algorithm 778: L-BFGS-B: Fortran subroutines for large-scale bound-constrained optimization, ACM Transactions on mathematical software (TOMS) 23 (1997) 550–560. doi:https://doi.org/10.1145/279232.279236.